Title

Lung parenchymal signal intensity in MRI: A technical review with educational aspirations regarding reversible versus irreversible transverse relaxation effects in common pulse sequences

Journal

Concepts in Magnetic Resonance Part A, 43A(2)

ISSN

1546-6086

Authors

Mulkern, Robert
Haker, Steven
Mamata, Hatsuho
et al.

Publication Date

2014-03-01

DOI

10.1002/cmr.a.21297

Peer reviewed

Published in final edited form as:
Concepts Magn Reson Part A Bridg Educ Res. 2014 March 1; 43A(2): 29–53. doi:10.1002/cmr.a.21297.

Lung Parenchymal Signal Intensity in MRI: A Technical Review with Educational Aspirations Regarding Reversible Versus Irreversible Transverse Relaxation Effects in Common Pulse Sequences

ROBERT MULKERN[1], **STEVEN HAKER**[2], **HATSUHO MAMATA**[2], **EDWARD LEE**[1], **DIMITRIOS MITSOURAS**[2], **KOICHI OSHIO**[2], **MUKUND BALASUBRAMANIAN**[1], and **HIROTO HATABU**[2]

[1]Children's Hospital, Radiology, Boston, MA, 02115

[2]Brigham and Women's Hospital, Radiology, Boston, MA, 02115

Abstract

Lung parenchyma is challenging to image with proton MRI. The large air space results in ~l/5th as many signal-generating protons compared to other organs. Air/tissue magnetic susceptibility differences lead to strong magnetic field gradients throughout the lungs and to broad frequency distributions, much broader than within other organs. Such distributions have been the subject of experimental and theoretical analyses which may reveal aspects of lung microarchitecture useful for diagnosis. Their most immediate relevance to current imaging practice is to cause rapid signal decays, commonly discussed in terms of short T_2^* values of 1 ms or lower at typical imaging field strengths. Herein we provide a brief review of previous studies describing and interpreting proton lung spectra. We then link these broad frequency distributions to rapid signal decays, though not necessarily the exponential decays generally used to define T_2^* values. We examine how these decays influence observed signal intensities and spatial mapping features associated with the most prominent torso imaging sequences, including spoiled gradient and spin echo sequences. Effects of imperfect refocusing pulses on the multiple echo signal decays in single shot fast spin echo (SSFSE) sequences and effects of broad frequency distributions on balanced steady state free precession (bSSFP) sequence signal intensities are also provided. The theoretical analyses are based on the concept of explicitly separating the effects of reversible and irreversible transverse relaxation processes, thus providing a somewhat novel and more general framework from which to estimate lung signal intensity behavior in modern imaging practice.

Keywords

magnetic resonance imaging; pulse sequence analysis; thoracic imaging; lung parenchyma; interstitial lung disease

Correspondence to: Robert Mulkern; rmulkern@yahoo.com.

INTRODUCTION AND MOTIVATION: IMAGING THE VOID

Figure 1 presents large field of view (FOV) 3 T coronal chest images in a subject with lung cancer. The two images were acquired using two common imaging sequences, a three-dimensional-FT T_1-weighted spoiled gradient echo sequence and a two-dimensional-FT single shot fast spin echo (SSFSE or HASTE) sequence. Note that the lungs appear as dark voids compared to other tissues like muscle, fat, and liver. Though some blood vessels may be seen scattered throughout the lung, the overall dark void provides a good background for visualizing water accumulation associated with pathological processes such as lung tumors. Images like these are acquired within breathholds in cooperative subjects and are useful in the detection and evaluation of so-called “positive” disease signs in which increased water content becomes conspicuous within the void. In such images, noise levels within regions of air outside of the body are similar to signal intensities within the lung parenchymal voids. These voids, however, are not completely devoid of signal, as demonstrated by the lung images of Fig. 2. Shown is a sagittal view through the chest of a healthy volunteer acquired with a single spin echo, multislice two-dimensional-FT imaging sequence acquired at 1.5 T during shallow breathing with a total acquisition time of 6.4 min. Two different window levels were used to display the same image in Fig. 2, one windowed for normal morphological inspection and the other windowed to highlight lung parenchymal signal where some inhomogeneity is observed as a consequence of gravitational effects leading to posterior water accumulation in the supine position. The pulse sequence details of the images in Figs. 1 and 2 are provided in the figure captions with the salient point here being that in order for us to visualize, albeit weakly, signal from lung parenchyma, a spin echo sequence with a long repetition time (TR) and a short echo time (TE) was required (Fig. 2). Further evidence that there is proton signal within the void of lung parenchyma is shown in Fig. 3 in the form of single voxel proton spectra in lung at 1.5 T and, for comparison, a spectrum from the liver of the same healthy 43-year-old male subject. The lung spectrum shows a broad, somewhat noisy, and asymmetric resonance in contrast to the narrow water and much smaller, lipid methylene resonance from the liver. The breadth of the water frequency distribution in lung parenchyma and its dearth of protons are both major factors in how the signal from lung behaves in common pulse sequences. Understanding this signal from the “void” motivates the technical analyses presented below in which both reversible and irreversible transverse relaxation effects are explicitly considered. This approach enables a more comprehensive understanding of the MRI signal from lung tissue whose clinical relevance may ultimately help optimize lung imaging for the detection of disease processes in which water signal is decreased as a consequence of alveolar thinning and/or airway expansions within the lung parenchymal space.

This article is organized as follows: we first review experimental and theoretical studies of lung parenchymal proton spectra. We then provide a review of what is known regarding general relaxation properties of the lung from imaging sequences designed to measure T_2, T_2*, and T_1. Then, a section devoted to exposing the relationship between inherent frequency distributions and resulting time domain signals is provided in which the effects of reversible and irreversible transverse relaxation mechanisms are evaluated. This is followed by considerations of the spatial mapping features in lung provided by frequency-encoding

readout gradients as calculated using the formalism of the preceding section to generate typical gradient echo and spin echo 1D projections as employed in two-dimensional and three-dimensional gradient and spin echo imaging sequences. A discussion of the single shot multiple spin echo approaches, SSFSE/HASTE sequences, is then provided. Specifically, analytic expressions for calculating echo amplitudes along the echo train in the presence of non-ideal 180° refocusing pulses are provided along with the interesting proposition that the echo maxima from lung parenchyma in such sequences should be similar to that from muscle tissue, albeit with a factor of 5 decrease due to its diminished proton density. Finally, a calculation of signal intensities to be expected from balanced steady state free precession (bSSFP) sequences is provided to examine how such parameters as flip angle, echo time, and repetition time affect the broad line signals from lung parenchyma.

THE LUNG PARENCHYMAL PROTON SPECTRUM

Air has no proton MR signal. Thus, the delicate, gossamer tissue structure of lung parenchyma is guaranteed to yield little MR signal compared to other, more solid organs, as may be gleaned from the torso images of Figs. 1 and 2. Furthermore, in solid organs like the brain, the role of intravoxel frequency distributions on signal intensities is relatively minor. For example, in typical brain voxels studied spectroscopically, water linewidths tend to be less than 0.5 ppm (5 to 30 Hz at 1.5 T), exceptions occurring near brain/bone and brain/air interfaces. In the lung, a much wider distribution of frequencies and frequency shifts is present due to its structure, which is composed of multiple “cells” of air coexisting with tissue constituents composed of lung parenchyma and major and minor blood vessels in close proximity to a powerful, beating heart muscle that sends motion-ghosted signals throughout the thorax. It is the large difference in magnetic susceptibility, approximately 8 ppm, between the air and tissue components of lung parenchyma that causes intravoxel broad frequency distributions. The air-filled alveoli act as magnetic perturbers of the local environment which, in conjunction with the complex geometry of the foam-like structure of the parenchyma, lead to a wide variation of microscopic magnetic fields and field gradients throughout the lung. These fields add to or subtract from the main magnetic field, resulting in a wide distribution of Larmor frequencies within any given voxel in a manner that is sensitive to the volume of air within the lung. But what exactly are these distributions and are they amenable to experimental estimation, theoretical simulation, and/or diagnostic interpretation?

These interesting questions have been partially answered since the mid 1980’s due to the sustained efforts of the Salt Lake City group from the University of Utah that provided a conceptual framework for lung parenchyma frequency distributions. In a series of original articles (1-7) whose contents were summarized in a 1996 textbook, *Application of Magnetic Resonance to the Study of Lung* (8), their work offers insights into how the unique Larmor frequency distributions in lung are generated by the complex tissue architecture and is based on fundamental magnetostatic considerations (9,10) for calculating field distributions within watery objects of various geometries immersed in large homogeneous magnetic fields. Working from the first principles supplied by Maxwell’s equations, field distributions from increasingly sophisticated geometries were calculated. The field distribution within a perfect sphere, for example, has a single unique frequency throughout its interior (2), offering a

convenient reference peak. A cube, on the other hand, shows a much more complex field distribution which depends on its orientation relative to the main magnetic field (4). Calculations of frequency distributions from more complex shapes designed to mimic the foam-like tissue architecture of the air-filled alveoli in lung were also considered (1-8). Hollow spherical shells with volume-filling air/tissue fractions from 0 to 0.74 and more sophisticated foam-like space-filling models based on Wigner-Seitz (WS) polyhedra capable of extending the air/tissue fraction from 0 to 1 were examined. Experiments performed in spectrometers and imaging equipment at a number of different field strengths using both simple geometric phantoms of spherical shells, rectangular slabs, and cubes, as well as inflated, excised rat lungs (7) provided frequency distributions, or spectral line shapes, which were largely consistent with the theoretical predictions. The most versatile theoretical tool for the more complicated space-filling foam structure models was based on a set of equations describing the field distribution of a rectangular slab as a function of its in-plane dimensions, its thickness, and its orientation to the main magnetic field (4,5). This tool allowed for the calculation of field distribution simulations for the space-filling WS polyhedral model and minor modifications (7). The sensitivity of such distributions to, for example, the thickness of the walls or the filling of the air spaces with water, as may occur in various disease processes, could thus be modeled. In addition, simulations with the WS model revealed a monotonic increase of the linewidth with increasing air volume (7). Finally, the nonparenchymal component of lung tissue, consisting primarily of small blood vessels, was modeled using cylinders and/or cylindrical shells, with these objects again demonstrating a profound orientation dependence which was averaged over random directions for realistic simulations of the nonparenchymal lung components (6,7).

Summarizing the findings of the lung frequency distribution studies, the combination of lung parenchyma and alveolar components yield a broad asymmetric line shape with a peak approximately –3 ppm to the left of a reference peak, based on a spherical object, and with a shoulder approximately 6 ppm to the right of the reference peak. The actual shape depends on the inflationary status. The overall width, or half width at half maximum (HWHM), of lung frequency distributions was shown to increase monotonically with the percentage of air and with field strength. Nonparenchymal cylindrical components, randomly oriented to the main magnetic field, yield a narrower line centered approximately 1.5 ppm to the right of the reference peak (6,7). Agreement between these theoretical predictions and experimental results from inflated, excised rat lungs were presented by the Salt Lake City group (6,7) and their findings were largely reproduced in humans in vivo independently by a Stanford group working with a short echo time spectroscopic imaging sequence at 1.5 T (11), reporting spectra similar to that acquired by us (Fig. 3), though we utilized a more pedestrian single voxel point resolved echo spectral (PRESS) sequence without a heroically short echo time.

Despite the demonstrated potential for spectral assessments to reveal geometric features of lung parenchyma that may prove useful for diagnosis, the measurement and use of spectra for clinical purposes remains elusive. Prolonged scan times and specialized pulse sequences (11-14) pose the usual difficulties not readily solved by dubious early efforts promoting two-point Dixon methods as a spectrally sensitive approach to lung parenchyma studies (12,13). The interesting relation between spectral line shapes and lung structure suggests that there may, in time, be significant value in clinical spectroscopic acquisitions. For now, however, it

is perhaps more important to ask how the intrinsic frequency distributions influence lung signal intensity and image quality from common pulse sequences currently used for thoracic imaging. A recent review of lung imaging with proton MRI (15) identified short echo time spoiled gradient echo imaging (SPGR) sequences (16), single shot turbo or fast spin echo (SSFSE, HASTE, etc.) sequences (17), and balanced steady state free precession (bSSFP) sequences (18) as the most relevant players. Thus, we now consider in detail how the broad frequency distributions inherent to lung parenchyma result in the observed signal intensities within these sequences. To achieve this goal, we use Bloch equation analyses of a single frequency, an "isochromat" w, and then extend these analyses to distributions of isochromats p(w). In particular, for gradient echo imaging we first demonstrate the fundamental relation between frequency distributions and T_2* decay, demonstrating how the conventional notion of a monoexponential signal decay with increasing gradient echo time is, in fact, a rather special case restricted to Lorentzian frequency distributions. We also examine how frequency distributions imposed by readout gradients in both gradient echo and spin echo imaging sequences compete with background frequency distributions when imaging lung by considering one-dimensional simulated projections across the torso, including simulated muscle tissue at the borders of the lung as encountered in practice. We then consider how the strong dephasing caused by readout gradients within SSFSE/HASTE imaging affects signal intensity along the multiple spin echo train and how the signal decay with echo number is affected by imperfect refocusing pulses introduced systematically to reduce specific absorption rate (SAR) and unsystematically through B_1 inhomogeneities encountered at higher field strengths like 3 T. Finally, a recently developed set of equations that extends the single isochromat bSSFP frequency dependence to a distribution of intravoxel frequencies is deployed to model bSSFP lung parenchymal signal. First, we review the lung-specific literature regarding longitudinal T_1 relaxation times, the two transverse relaxation times T_2 and T_2*, and the related reversible relaxation time T_2'.

RELAXATION PROPERTIES OF LUNG TISSUE FROM IMAGING STUDIES

We begin with a discussion of transverse relaxation in which care is taken to distinguish irreversible from reversible transverse relaxation mechanisms, a step towards understanding the difference between the commonly used terms T_2 and T_2*. The relaxation time referred to as T_2 is associated with the "irreversible" relaxation processes that occur regardless of manipulations applied in the form of full or partial RF refocusing pulses. These processes arise from dynamic, random fluctuations in time of the microscopic magnetic fields experienced by individual spins, primarily from neighboring spins. Tumbling of water molecules and interactions of water with proteins, macromolecules, and membranes all lead to magnetic field fluctuations at or near the Larmor frequency which then cause both irreversible T_2 relaxation and longitudinal, or T_1, relaxation. Such processes ensure that once a coherent precession of spins within a voxel is initiated by an "excitation" pulse, the coherence will vanish with time and the excited magnetization will return to its equilibrium configuration along the axis of the main magnetic field via T_1 relaxation. The irreversible dephasing is not disturbed by the application of refocusing pulses often used to solicit spin echoes. The maxima, or the centers of successive spin echoes, are generally assumed to decay exponentially with the irreversible relaxation rate $R_2 = 1/T_2$, though multiple water

compartments with distinct T_2 values within them can lead to multiexponential T_2 decays within lung parenchyma as reviewed further below.

In contrast to the irreversible relaxation mechanisms reducing the amplitudes of RF refocused spin echoes, there are so-called "reversible" transverse relaxation processes that are indeed reversed, or restored, by refocusing pulses. The reversible dephasing processes are associated with static or very low frequency microscopic magnetic fields and/or field gradients that may exist within a voxel by happenstance or design, the latter occurring when we apply imaging gradients, for example. These static fields cause a natural dephasing of spins that is, or can be, partially refocused with appropriate RF pulses. The wider the distribution of static magnetic fields within a voxel is, the faster the intravoxel dephasing due to the reversible relaxation processes will be, with an analogous "exponential" relaxation decay rate $R_2' = 1/T_2'$ occurring in the case of a Lorentzian distribution of frequencies, as we prove below.

A useful analogy for obtaining a qualitative understanding of the differences between reversible and irreversible transverse relaxation is that of a horse race. One can imagine a race in which horses start running at distinctly different, but constant, speeds. The horses would fan out, or "dephase" as the race proceeds in an orderly fashion and if, by magic, they could be instantly turned around (gradient echo) or instantaneously placed at mirrored positions with respect to the starting line (spin echo), then the fast horses would be behind the slow horses and they would all catch up at the starting line, fully "rephased." The horses all running at constant but different speeds represent a fully reversible situation and so are analogous to reversible transverse relaxation processes. Obviously, horses do not run in that manner. They may jostle one another, get tired or get motivated and slow down or speed up as the race progresses, all in a manner that guarantees that the second, or rephasing, half of the race will be somewhat different from the first, or dephasing, half of the race. The random adjustments to the "constant" speeds of the horses are analogous to the irreversible transverse relaxation processes and ensure that the horses do not fully rephase at the starting line. Though somewhat simplified, the horse race analogy loosely explains the link between broad frequency distributions (a wide variation in constant horse speeds) and the short lung T_2^* values (rapid dephasing) as measured by several groups (19-25). Let us review these reports as well as studies designed to measure the irreversible relaxation rate R_2 (17,26-29), beginning with the latter.

In a study of lung parenchyma signal in 10 healthy volunteers at 1.5 T acquired with two different cardiacgated, T_1-weighted, single spin echo or "Hahn spin echo" sequences, Mayo et al. determined that the signal at a TE of 7 ms was significantly larger than signal acquired at a TE of 20 ms (26). Though specific T_2 values were not reported, Table 1 from that study provides the means to calculate them, and they lie between 12 and 15 ms. The same group, however, measured T_2 values in an in vitro model of juvenile pig lungs at 1.5 T with a multi-echo Carr-Purcell-Meiboom-Gill (CPMG) sequence using 16 echoes with a 10 ms echo spacing (27), reporting multiexponential relaxation decay curves with longer T_2 values. Specifically, in inflated lungs three T_2 components were observed with values of 18, 59, and 206 ms with relative volume percentages of 41, 53, and 6% respectively. The three T_2 values became significantly prolonged in deflated lungs (27). Overall, their results were

consistent with in vivo (28) and in vitro (29) T_2 studies of rat lungs using Hahn spin echo and multi-echo CPMG sequences. Furthermore, using cardiac-triggered SSFSE/HASTE sequences, Hatabu et al. reported relatively long T_2 values of 60 to 100 ms *in vivo* in humans (17). In that study, the effective TE's covered a range of values from 26 to 60 ms, significantly longer than the single, shorter TE's used by Mayo et al. (26) with the combined results from both studies proving consistent with multiexponential T_2 decays within lung parenchyma.

Clearly, the actual T_2 behavior in lung parenchyma is complicated, consisting of multiple T_2 components. Furthermore, the T_2 values measured will depend upon the methods used to measure them as well as the degree of lung inflation. In particular, the fact that longer T_2 values are found when multiple spin echo sequences are used is consistent with bodily spin motion, e.g. perfusion and/or diffusion, within the background microscopic field gradients created by the multiple air/tissue interfaces within lung parenchyma, as discussed in the original articles (3,26-29). This same mechanism is most probably responsible for later observations by Ohno et al. of an inter echo spacing dependence of lung signal from SSFSE/HASTE sequences (30). Specifically, they demonstrated that shorter echo spacings lead to larger signal even at similar, fairly long effective echo times (ETE's) of around 40 ms. The mechanism postulated for this observation, perfusion/diffusion within background and/or imaging gradients, is discussed in further detail below in the context of SSFSE/HASTE signal intensities. Parenthetically, T_1 relaxation is not expected to be affected by this mechanism. Indeed, Estilaei et al. (27) measured T_1 within in vitro pig lungs at 1.5 T to be on the order of 1 s, a generic value similar to many other tissues, including muscle. Earlier studies of in vitro animal lung tissue (3) showed increasing T_1 with field strength, as also occurs in other organs. In vivo studies in humans on clinical scanners at 1.5 T by Edelman et al. (31) and Stock et al. (32) initially reported T_1 values on the order of 900 ms with significant reductions toward 775 ms possible by introducing oxygen-enriched breathing gas as a paramagnetic contrast agent. Mai et al. (33) subsequently reported higher T_1 values around 1,400 ms in human lung at 1.5 T, explaining the discrepancy with the earlier reports as possibly due to the use of slice-selective versus non-slice-selective inversion pulses employed for measurement with the subsequent introduction of in-flowing blood effects in the former case. In any event, they succeeded in demonstrating increased parenchymal visualization with the use of two inversion pulses applied prior to SSFSE/HASTE acquisitions at inversion times (TI) of 800 ms and 150 ms to null muscle and fat respectively. Although the T_1-weighting provided by the inversion pulses reduces the signal from lung parenchyma by some 80% (33), the nulling of signal from proton-rich muscle and fat tissues in the torso proved useful in later studies for visualizing gravitational dependent parenchymal signal gradients (31) and differences in expiration vs. inspiration parenchymal signal changes in healthy subjects vs. those with chronic obstructive pulmonary disease (COPD) (34).

To summarize, the T_2 and T_1 properties of lung parenchyma are not much different from many other tissues, as shown in Table 1, which lists generic values at 1.5 T for parenchymal and nonparenchymal lung tissue and other tissues found in torso imaging, i.e. muscle, fat, and blood in large vessels. The proton density (PD) of lung (relative to other tissues taken as

unity) is a factor of 5 or so lower than the other tissues, leading to a big difference in signal intensity. However, the final columns of Table 1 reveal that the largest difference between lung tissue and other tissues lies in its T_2* value, which is much shorter than that of other tissues. The contemporary T_2* lung studies that revealed this feature by Hatabu et al. (19) and Stock et al. (20), utilized multiple gradient echo acquisitions at 1.5 T to gather data sets suitable for measuring the decay of healthy lung parenchymal signal for very short echo times ranging from less than 1 ms to several ms. Fitting the decay curves with monoexponential decay functions led to T_2* values of 0.8 to 2 ms with regional variations reported as well as variations between maximum expiration and inspiration, the former yielding more signal as anticipated from earlier studies (6,7). The TE = 0 intercepts of decay curves were also used to estimate proton densities relative to muscle tissue and showed an anterior-posterior proton density gradient that could be reversed when going from the supine to prone position, indicating gravitational effects (19). The use of detailed gradient echo signal decays to estimate proton density, and thus lung water content (35), may have important diagnostic implications in a number of diseases, including COPD and cystic fibrosis. Indeed, Ohno et al. demonstrated the feasibility of making ultra-short TE gradient echo acquisitions (0.2 ms to 4.7 ms) even at 3 T to measure T_2* in smokers, potentially offering an assessment of clinical stage classification (22). Theilmann et al. stressed the importance of the inflationary state of the lung in making T_2* and associated lung water density measurements at 1.5 T (21), while Yu et al. more recently measured T_2* in lung parenchyma at 1.5 T and 3 T, pointing out that normal free breathing has a small effect on the T_2* values compared to the full inspiration/expiration extremes (23). In this latter study of five healthy volunteers, the 3 T T_2* values were found to be nearly three times smaller than those measured at 1.5 T, with average values of 0.74 ms and 2.11 ms at the two field strengths respectively. Finally, in a bSSFP study of lung perfusion at 0.2 T discussed further below, Martirosian et al. measured and compared T_2* values with multiple gradient echo acquisitions at 0.2 T and 1.5 T at both inspiration and expiration (24). Values at 0.2 T for T_2* were in the 7 to 9 ms range while those at 1.5 T were consistent with other studies having T_2* values on the order of 0.6 to 2 ms. Given the low signal-to-noise and the fairly large regional variation of T_2* in human lungs, the measurements over the last 10 to 15 years tend to support at least a linear increase of $1/T_2$* with field strength, according to Yu et al. possibly more due to the diffusion/perfusion mechanism in background gradients (23). The findings in humans regarding field strength and inflationary status are consistent with the experimental and theoretical spectral considerations forwarded by the Salt Lake City group prior to these more contemporary studies made possible by faster switching gradients and advanced pulse sequence designs allowing for ultra-short echo times on clinical scanners.

Table 1 not only summarizes approximate relaxation properties and characteristics of key tissue components in the torso as gleaned from the literature, primarily from 1.5 T studies, but also provides the generic set of relaxation parameters that we will use in signal simulations below. For the two lung components, parenchyma and nonparenchymal tissues, a longitudinal relaxation similar to many other tissues with $R_1 = 1\ s^{-1}$ will be employed, while for R_2 we shall employ $25\ s^{-1}$. This value for R_2 obviously will not reflect the complicated multiexponential nature of the T_2 decay nor the echo spacing dependence (vide

supra), features that could be incorporated into the simulations once more refined estimates of these effects have been documented. For Lorentzian distribution considerations (vide infra), R_2' values for parenchymal and nonparenchymal components are assigned to be 1,000 and 100 s^{-1}, respectively, which with the R_2 values of 25 s^{-1} lead to T_2* values of 1 and 8 ms, respectively. Objects in nature that share the unique lung relaxation properties include apples and sponge material as shown in Fig. 4. These objects were imaged with a gradient echo train and a CPMG echo train at 1.5 T, demonstrating relatively long T_2 values compared to their very short T_2* values, separated by over an order of magnitude (details provided in figure caption).

What all the previous studies of lung relaxation have in common is the orthodox, if useful, approximations employed when using either spin or gradient echoes. Namely, the signal decay weighting for a gradient echo is assumed to be of the form exp (–TE R_2*) while that for a spin echo is exp(–TE R_2), and overall the signal for spoiled acquisitions takes on a T_1 relaxation weighting of the form (1 – exp(–TR R_1)) with appropriate modifications when inversion recovery (IR) pulses are applied as in short T_1 inversion recovery (STIR) sequences for fat reduction or the double IR technique for nulling muscle and fat signals (33-36). Focusing on the transverse relaxation approximations, it is often stated that the link between T_2 and T_2*, or more appropriately, their associated relaxation rates R_2 and R_2*, is given by $R_2^* = R_2 + R_2'$ where R_2' is the reversible relaxation rate associated with the static distribution of frequencies within a voxel. We now demonstrate that R_2* as the sum of the reversible and irreversible relaxation rates is valid only for the case of a Lorentzian distribution of frequencies but that more generally this simple relation does not hold, and a more nuanced approach to reversible relaxation is called for. Namely, we examine in greater detail the effects of the widths and central frequencies of intrinsic frequency distributions $p(w)$ within a voxel.

FREQUENCY DISTRIBUTIONS AND TIME DOMAIN SIGNALS

Consider three distributions with well-defined central frequencies w_o and well-defined widths: the Lorentzian distribution, the Gaussian distribution, and a Uniform distribution, all suitably normalized for the moment such that integration over all angular frequencies w leads to unity. These read:

$$Lorentzian: p(w) = (R_2'/\pi)/[(w-(w_o+iR_2'))(w-(w_o-iR_2'))] \quad [1]$$

$$Gaussian: \quad p(w) = (\sigma(2\pi)^{1/2})^{-1} exp\,(-(w-w_o)^2/2\sigma^2) \quad [2]$$

$$Uniform: 0 \; for \; w < w_o - \Delta w$$

$$p(w) = 1/(2\Delta w) \; for \; w_o - \Delta w < w < w_o + \Delta w$$
$$0 \; for \; w > w_o + \Delta w. \quad [3]$$

Other distributions are possible including asymmetric distributions (37). However, the three symmetrical distributions above are commonly encountered in the field and often closely

approximate physically realistic situations arising in the magnetic resonance environment. In addition, they share the convenient property of allowing for analytic integration where required. Figure 5 (top left) shows each of the three distributions with effectively equivalent linewidth parameters of 1,000 Hz and all centered at 0 Hz. The parameter R_2' reflects the width of the Lorentzian function where the full width at half maximum (FWHM) is $2R_2$' while σ reflects the width of the Gaussian with FWHM being ~2.35 σ. The parameter Δ*w* reflects the width of the Uniform function where the FWHM is simply 2Δ*w*. Note that all these width parameters are referenced to the angular frequency w so that if a FWHM is reported in frequency units, a π will be involved in converting FWHM to a relaxation rate or time. For example, at 1.5 T Martirosian et al. reported ventral lung FWHM at inspiration to be 277 Hz or an equivalent R_2' of $\pi \times 277 = 870\ s^{-1}$ which in the limit of $R_2' \gg R_2$ yields a T_2* value on the order of 1.1 ms (24), consistent with other 1.5 T studies (19-21).

In the context of MRI, the Lorentzian and the Gaussian frequency distributions may be thought of as simulating inherent, or background, frequency distributions present within any imaged voxel. Inherent frequency distributions such as the uniform pattern are also possible near tissue interfaces but are also realistic depictions of the distributions from frequency-encoding gradients across a voxel that we will consider as well. To examine how the shape and widths of these distributions affect signal and, in particular, reflect the reversible relaxation processes, the following specific procedure is performed: First, a Bloch equation analysis of any given sequence or sequence element is performed to determine the three components of the magnetization vector *f*, *g*, and *m* and, in particular, the transverse magnetization *f* + *ig*, or "signal", as a function of time *t* for any given isochromat *w*. The only tools used for this step are the standard rotation matrices representing instantaneous effects of RF pulses with specific flip angles around the *x*-axis or *y*-axis and a free precession matrix with angular frequency w about the *z*-axis and with the irreversible transverse relaxation rate R_2 and longitudinal relaxation rate R_1 included, as detailed in the Appendix. Then, a mathematical step is performed to incorporate any desired distribution *p*(*w*) to reveal the effects of the reversible transverse relaxation. Namely, the pulse sequence-specific expression for the signal during readout time *t* is multiplied by a frequency distribution *p*(*w*) and then integrated over all real *w*. In this manner, a time domain signal that includes all the effects of both reversible and irreversible transverse relaxation processes, resonance offsets, and T_1 relaxation is derived. As we shall see, the parameters reflecting the widths of the frequency distributions dominate the reversible relaxation processes. Integrals involving the Lorentzian distribution are most conveniently carried out using contour integration, evaluating the residues from the poles apparent in Eq. [1] at $w = w_o + i\,R_2$' or $w = w_o - i\,R_2$' in the upper and lower halves of the complex plane, as appropriate (40). Integrals involving the Gaussian distribution will require the relation (41):

$$\int exp\,(-p^2x^2 \pm qx)dx = ((\pi)^{1/2}/p)\,exp\,(q^2/4p^2)\,for\ Re\,p^2>0 \quad [4]$$

and integrals associated with the Uniform distribution rather trivially lead to sinc type functions as detailed below.

This analytical approach is first applied to the free induction decay (FID) signal following a single excitation repeated at intervals of τ, perhaps the simplest of all MR experiments and

one that represents how signal from a gradient echo sequence with increasing echo times will behave. For a single RF pulse of flip angle a applied along the x-axis of the rotating frame followed by a readout time *t*, the a_x–*t* sequence, with imaging gradients ignored but assuming that gradients and RF spoiling have been used so that prior to each RF pulse the transverse magnetization components are absent or "spoiled," we have that at $t = 0$, immediately prior to each pulse, the steady state longitudinal magnetization m_o is given by:

$$m_o = m_{oo}(1 - exp(-R_1\tau))/[1 - cos\alpha\ exp(-R_1\tau)] \quad [5]$$

where m_{oo} is the equilibrium longitudinal magnetization (taken as unity throughout) and τ is the total time between consecutive RF pulses. We act upon this magnetization with an a_x pulse, treated as the standard rotation matrix about *x* (see Appendix). This is followed by free precession by w about the z-axis and classic T_1 and T_2 relaxation (see the precession/relaxation step in the Appendix). The resulting expression for the transverse magnetization *f* + *ig* during the readout time *t* is found to be:

$$f + ig = m_o sin\alpha\ exp(-R_2 t)\ exp(-iwt). \quad [6]$$

This expression contains the longitudinal and irreversible transverse relaxation dependencies for a single isochromat *w*. To determine the reversible transverse relaxation dependence we now consider our list of three potential frequency distributions above, multiplying Eq. [6] by each *p*(*w*) followed by integration over all real *w*. For the Lorentzian distribution we find the signal to be given by:

$$(f + ig)_{Lor} = m_o sin\alpha\ exp(-iw_o t)\ exp(-(R_2 + R_2')t). \quad [7]$$

This expression is probably the simplest and most widely used formula for describing T_2^* relaxation phenomena where the FID decays with time *t* according to the sum of the irreversible and reversible relaxation rates $R_2 + R_2' = R_2^* = 1/T_2^*$. Despite its widespread and ubiquitous usage, Eq. [7] pertains strictly to the special case of Lorentzian frequency distributions. For the Gaussian distribution, our procedure leads to a rather different expression for the FID:

$$(f + ig)_{Gauss} = m_o sin\alpha\ exp(-iw_o t)\ exp(-R_2 t)\ exp(-\sigma^2 t_2/2) \quad [8]$$

while for the Uniform distribution we find:

$$(f + ig)_{Uniform} = m_o sin\alpha\ exp(-iw_o t)\ exp(-R_2 t)\ sin(\Delta w t)/(\Delta w t). \quad [9]$$

The time domain signals resulting from each of the three different frequency distributions of Fig. 5 (top left), with an irreversible relaxation rate $R_2 = 25$ sec $^{-1}$ and $w_o = 0$ rad/sec, are provided in the top right of the figure. Only for the Lorentzian case does the signal show a purely exponential decay with time *t*. For the Gaussian distribution, an exponential decay at the irreversible transverse relaxation R_2 is modulated by a Gaussian decay from the

reversible transverse relaxation process whereas for the Uniform distribution a sinc function modulation sin(Δ*wt*)/(Δ*wt*), is observed. The lower left of Fig. 5 shows how a simple sum of two distributions can mimic lung spectral line shapes produced by the calculated WS foam model shapes (see Fig. 4 in Ref. 6) and the lung spectrum in Fig 3. The distribution in the lower left is the sum of a Lorentzian distribution (green curve) and a Gaussian distribution (blue curve) 1/10 its size and centered 240 Hz to its right. The spectrum displays an asymmetric shape similar to spectra calculated from first principles with the WS foam model and to the lung spectrum in Fig 3. The spectrum is not intended to represent an actual fit to either the WS model or the experimental spectrum but is intended to demonstrate how these simpler distributions have the ability to represent key aspects of lung spectra and may be used to analytically calculate the resulting FIDs, as shown in the lower right panel of Fig 5.

Similar analyses are repeated below for more complex sequences. Each time the effects of reversible and irreversible transverse relaxation processes are separately evaluated, as in the spin echo case discussed by Ma and Wehrli several years ago (42). Though the approach quite naturally includes the effects of central frequency offsets and widths of frequency distributions while also incorporating T_1 and irreversible T_2 relaxation effects, there are still several approximations involved. Namely, relaxation during RF pulses (43), flow, diffusion, and gross motion have not been considered, though such effects can be included. Furthermore, the formal separation of transverse relaxation into two extremes, reversible and irreversible, is questionable for some processes like water diffusion within background and/or imaging gradients.

GRADIENT AND SPIN ECHO READOUT CONSIDERATIONS

Now we examine how the background frequency distributions in lung will affect the basic frequency-encoding readouts used in both gradient echo and spin echo acquisitions. Such readouts are an essential aspect of imaging, or spatial encoding, in MRI and require the use of magnetic field gradients applied during the “listening” or “reading” of time domain signals like those shown in Fig 5. In one sense, a readout gradient may be considered a “reversible” relaxation mechanism and so may be treated with the same general formalism applied throughout this work. The detailed analysis provided by this approach lets us examine the quality of the spatial mapping obtainable with frequency encoding in the presence of broad spectral components as found in lung parenchyma.

We used the tools described in the appendix to calculate the signal $S = f + ig$ during time t from a gradient echo $\theta_x - \tau - t$ sequence in which a frequency-encoding gradient of amplitude $-G$ is applied along the x-axis during τ and is then reversed to $+G$ during t. In practice, most gradient echo sequences use a stronger gradient during τ than during t. This would make the math slightly more complicated without any great gain in generality so we proceed with the sequence proposed and find that the signal S for an isochromat w is given by:

$$S = i\, m_o \sin\theta \exp\left(-iw(\tau+t)\right) \exp\left(iG\gamma x(\tau - t)\right) \exp\left(-R_2(\tau+t)\right) \quad [10]$$

where m_o is the longitudinal magnetization prior to the θ_x pulse and γ is the gyromagnetic ratio for protons ($2\pi \times 4{,}258$ Hz/Gauss). For exemplary purposes, we now consider a simple step function spin density $p(x)$ along the x direction where $p(x)$ is unity along the interval $x_o \pm \Delta x_o$ and 0 everywhere else. We further assume a proportionality between $m_o(x)$ and $p(x)$ and heuristically replace m_o with $p(x)$ in Eq. [10]. Integration of S over x with the "box" $p(x)$ distribution leads to the signal that is received, recorded, and then Fourier transformed (FT) over t during image reconstruction. This signal reads:

$$S = 2\sin\theta \exp(-iw(\tau+t)) \exp(iG\gamma x_o(\tau - t)) \sin(G\gamma\Delta x_o(\tau - t)) \exp(-R_2(\tau+t))/[G\gamma(\tau - t)]. \quad [11]$$

Note the appearance of the sinc-like function associated with the integration over x, as the readout gradient across a voxel is equivalent to the use of Uniform distribution considered for a reversible process, as discussed in the preceding section. Eq. [11], however, now also puts us in a position to determine how an inherent background frequency distribution p(w) within a voxel along p(x) will affect the signal. Multiplying Eq. [11] with, for example, a Lorentzian function followed by integration over w leads to:

$$S_{Lor} = 2\sin\theta \exp(iG\gamma x_o(\tau - t)) \sin(G\gamma\Delta x_o(\tau - t)) \exp(-(R_2+R_2')(\tau+t)) \exp(-iw_o(\tau+t))/[G\gamma(\mathrm{t} - t)]. \quad [12]$$

Equation [12] contains the effects of both readout gradients and background frequency distributions and allows us to evaluate how the inherent distributions within the lung affect the mapping of the spin density $p(x)$ via frequency encoding. Simulations using Eq. [12] with R_2' values of 100 s^{-1}, for nonparenchymal lung tissue components, and 1,000 s^{-1}, for parenchymal lung tissue, using a relatively short τ value of 1 ms, corresponding to a TE of 2 ms, are shown in Fig. 6 (top row) along with their respective Fourier transforms (bottom row) corresponding to a 4 cm segment of lung tissue centered at $x = 0$. Parameters for these simulations included an R_2 value of 25 s^{-1}, readout gradient strength G of 1.5 Gauss/cm, and 256 samples of the echo with a ±64 kHz receiver bandwidth corresponding to a "dwell time" of 7.8 μs and a full echo readout time of 2 ms. The FT operation is performed numerically as described previously (44). Note how for the slower R_2' of 100 s^{-1} simulation a fairly symmetric echo signal (top left) is observed with a median signal intensity (lower left) some five times higher than the signal intensity of the 1,000 s^{-1} simulation (lower right). There is also an observable asymmetry of the high R_2' echo (top right) with reduced signal at later readout times, leading to increased edge artifact in the projection (lower right). These are the explicit effects of broad distributions on signals and their Fourier transforms used for spatial mapping, highlighting the need for short echo times and fast sampling (high receiver bandwidths) for gradient echo imaging of lung tissue at high field strengths.

A similar calculation for the spin echo sequence $90_y - \tau - 180_y - t$ with the readout gradient G applied positively throughout both τ and t intervals leads to a readout signal during time t after the 180° pulse of:

$$S = m_o exp\,(-R_2(\tau+t))\; exp\,(iw(\tau - t))\; exp\,(i\gamma G x(\tau - t)) \quad [13]$$

which we can then integrate over x using a step function distribution and w using, for example, the Lorentzian distribution, as we did above for the gradient echo to obtain

$$S_{Lor} = 2\; exp\,(iG\gamma x_o(\tau - t))\; sin\,(G\gamma \Delta x_o(\tau - t))$$
$$exp\,(-R_2(\tau+t))\; exp\,(-R_2'\,|\tau - t|)\; exp\,(iw_o(\tau - t))/[G\gamma(\tau - t)]. \quad [14]$$

Equation [14] is a fascinating equation—it specifically defines the "first-half" of an echo prior to the magical time $t = \tau$ and the "second-half" of the echo for $t > \tau$. The absolute value symbols in the argument of the R_2' exponential term guarantee that for $t < \tau$, the total transverse relaxation is governed by the term $\exp(-(R_2 - R_2')t)$ so that if $R_2' > R_2$ the "decay" is actually a growth of signal. This is clearly the case in the lung where R_2' greatly exceeds R_2 but not the case for muscle where $R_2' < R_2$. The interesting feature of the first-half of a spin echo is that the irreversible mechanisms of transverse relaxation compete with the reversible mechanisms of transverse relaxation and occasionally lose, as in the lung. For $t > \tau$, they work together and the combined transverse relaxation is governed by the pure decay $\exp(-(R_2 + R_2')t)$ just as in the FID case discussed above. Of course all these statements must be slightly recast for different distributions such as the Gaussian or the step function but the same qualitative behavior ensues with the widths of the distributions replacing the R_2' of the Lorentzian. It is the growth of signal with $R_2' > R_2$ in the lung for $t < \tau$ that restores signal from spin echoes compared to gradient echoes and allows for the use of spin echo acquisitions for lung parenchymal signal intensity measurements even at echo times that greatly exceed the very short echo times used for gradient echo imaging of lung at 1.5 T and higher. Fig. 7 presents simulated profiles reconstructed using the FT of a gradient echo signal (top) and a spin echo signal (bottom) of lung parenchyma (blue) sandwiched by muscle tissue (red) in which the lung signal has been divided by a factor of 5 to account for the reduced proton density. The echo times of the gradient echo and spin echo acquisitions were 2 and 10 ms, respectively. Despite the 5× longer echo time of the spin echo, substantial signal from lung parenchyma is retained. This refocusing of signal by 180° pulses is the reason why one can actually utilize SSFSE/HASTE approaches for lung parenchymal imaging (17,30), as now discussed.

SSFSE/HASTE SEQUENCES

Single shot turbo or fast spin echo (SSFSE/HASTE) sequences (17) apply multiple slice-selective RF refocusing pulses following a slice-selective excitation. The use of anywhere from 70 to over 100 refocusing pulses, in combination with half-Fourier techniques (45,46), yields enough echoes to fill *k*-space in a single shot, e.g., one TR, minimizing motion related artifacts. The fundamental tradeoff with this "snapshot" imaging technique lies in the fact that the echo signals successively diminish due to, for perfect 180° refocusing pulses, T_2 decay. The longer the echo train, the less signal in later echoes leading to different *k*-space lines having different signal weightings. The tradeoffs between tissue contrast and blurring, edge definition artifacts and the phase-encode ghost noise levels associated with this "*k*-space filter" were discussed extensively in the early 1990s (44,47-52) as the methods began

to globally replace conventional spin echo imaging. Briefly, artifacts appear along the phase-encode direction and depend upon the precise order in which the distinct phase encodes are arranged within the echo train. The effective echo time (ETE) from the T_2 standpoint of tissue contrast occurs around the echo time(s) endowed with the smallest phase-encode gradients, or the central lines of *k*-space (44). With SSFSE/HASTE methods, the long echo trains required mean that all the artifacts associated with the decay of successive echoes are maximized to obtain the "snapshot" imaging. Thus, efforts are made to keep the echo trains as short as possible while retaining sufficient signal-to-noise and spatial resolution using half-Fourier approaches (45,46) and, more recently, parallel imaging methods with multiple RF receiver coils (53,54). Also, echo spacings are minimized using high receiver bandwidths and strong readout gradients; the latter impart a wide distribution of frequencies across each voxel, even wider than the inherent frequency distributions in the lung. This results in a fully dephased transverse magnetization prior to each refocusing pulse. The combination of short duration RF pulses and inherent frequency distributions obviously makes it difficult or impossible to achieve 180° refocusing effects across entire FOVs for all slices. Furthermore, nominal refocusing pulse flip angles (FAs) less than 180° are generally prescribed to reduce the SAR. Thus, it can be assured that the decay of signal during SSFSE/HASTE acquisitions will be somewhat more complicated than simple T_2 decay as assumed in previous artifact studies. Therefore, rather than reiterating the early literature on how T_2 decay influences the image quality aspects along the phase-encode direction (47-52), we focus our attention on simulating realistic echo train decays that include the effects of dephasing from readout and/or inherent frequency distributions in the lung and non-ideal refocusing pulses. This analysis, largely unexplored to date, may prove useful in arriving at a more detailed description of the k-space filter effect on image quality and reducing phase-encode ghosting, which will interfere with parenchymal signal intensity measurements. Of interest as well is that the approach outlined below can be used for variable flip angle refocusing methods designed to "level out" the echo signal decays as previously shown in brain imaging applications (55,56), again in an effort to improve visualization of lung parenchyma with SSFSE/HASTE sequences.

To simulate echo train decays in detail, we consider the fundamental segment of a fast spin echo (FSE) sequence from the center of one spin echo to another ($\tau - \theta_y - \tau$) and find that the magnetization components of echo number $n + 1$ are related to those at echo number n via the relation:

$$\begin{pmatrix} f_{n+1} \\ g_{n+1} \\ m_{n+1} \end{pmatrix} = \boldsymbol{A} \begin{pmatrix} f_n \\ g_n \\ m_n \end{pmatrix} + \mathbf{B} \quad [15]$$

where $\boldsymbol{A}$ is a 3 × 3 matrix and $\mathbf{B}$ a 3 × 1 vector whose specific elements are provided in the appendix. Using this formalism it is easy to show that if the initial magnetization following an excitation pulse is $(f_o, g_o, m_o)^T$ then the magnetization at the center of the readout following the *n*th refocusing pulse is given by:

$$\begin{pmatrix} f_N \\ g_N \\ m_N \end{pmatrix} = \mathbf{A}^N \begin{pmatrix} f_o \\ g_o \\ m_o \end{pmatrix} + \sum_{n=0}^{N-1} \mathbf{A}^n \mathbf{B} \quad [16]$$

Equation [16] is applicable to a single isochromat w so that, for each echo signal, we will need to consider an appropriate frequency distribution $p(w)$ and numerically integrate over w, noting that analytic integration of such exepressions even for a very small number of refocusing pulses would be effectively intractable. The formalism of Eqs. [15] and [16] coupled with numerical integration over w is, however, quite suitable for generating simulations of the magnetization at echo center with increasing echo number for different frequency distributions and refocusing flip angles, as shown in Figs. 8 and 9 where we used the lung parenchymal relaxation parameters $R_1 = 1\ s^{-1}$ and $R_2 = 25\ s^{-1}$ and an echo spacing 2τ of 5 ms. Figure 8 shows the three components of the magnetization as evaluated at each echo center within a 128 echo train for the case of a perfect $90_x°$ excitation pulse and for refocusing pulse FAs of 130°. The starting magnetization for this case is precisely along the y-axis of the rotating frame so that g (green) begins as unity, and f and m (blue and magenta) are 0 following initial excitation. Two off-resonance cases are shown, one for a narrow distribution of on-resonance spins (top row) and the other for spins with a narrow set of resonance frequencies that lead to a phase offset of $\pi/2$ prior to each RF pulse (bottom row). In the on-resonance case, the so-called CPMG condition exists such that the refocusing pulses are always aligned along the y-magnetization in the rotating frame. The result (top row) is that the magnetization vector at each echo center remains within a small cone around the y-axis of the rotating frame, explaining the very small deviations of the x-and z-magnetizations with echo time in the top row of Fig. 8. What deviations in x- and z-magnetizations that do exist are attributable to a very small amount of T_1 relaxation occurring between pulses at these parameter settings. In this case, even though the FA is 130° as opposed to 180°, the y-magnetization shows a smooth exponential T_2-decay, explaining why the 90° phase shift between excitation and refocusing pulses, the so-called Meiboom-Gill (MP) modification to the Carr-Purcell (CP) multi-echo sequence which used identical phases for all RF pulses, was introduced so long ago (57). In the particular off-resonance case considered here (bottom row of Fig. 8), the worst case scenario is visited, in which the first refocusing pulse is now aligned along an axis (the y-axis) perpendicular to the magnetization which has evolved to the x-axis of the rotating frame. This is equivalent to on-resonance spins in the CP sequence in which imperfections in FA become most pronounced, leading to the large oscillations in the decay curve of the y-magnetization and similar oscillations in the z-magnetization with echo number (bottom row). Conceptually in this case, the magnetization vector immediately following each refocusing pulse lies largely within the x–z plane of the rotating frame, with the transverse component evolving to the y-axis at echo center. This explains negligible deviation of the x-component of the magnetization with echo number and the rather unruly T_2 “decay curve” for the y-magnetization which would have serious effects on image quality via oscillations in the resulting lines of k-space in HASTE/SSFSE acquisitions. In reality, however, neither on-resonance (CPMG) or worst case off-resonance (CP) conditions apply in HASTE/SSFSE imaging as the strong readout gradients for all tissues, and the additional background

frequency distributions in lung, lead to a wide distribution of phases within each voxel prior to each refocusing pulse. We now consider echo time evolution when such wide distributions are present, as for example a step distribution of phases from $-\pi/2$ to $\pi/2$ prior to the first refocusing pulse. Using the formalism of Eqs. [15] and [16] with a numerical integration over this distribution leads to relatively smooth, and somewhat similar, decay curves for different FA values of 180°, 130°, and 90° as shown in Fig. 9. Note that only with ideal 180° refocusing pulses (top left, Fig. 9) is a perfectly smooth T_2 decay observed. In the other cases, jagged decays are seen with the first echo signal actually lower than the second. Such effects can be expected to lead to minor artifacts not considered in the earlier literature on blurring and edge definition (47-52) but which will affect actual SSFSE/HASTE imaging, though equally for lung tissue and other torso tissues like muscle. In general, however, despite the small differences among the signal "decays" in Fig. 9, there is an overall similar behavior, underscoring the well-known resilience of SSFSE/HASTE-type sequences to refocusing pulse variations and intrinsic frequency offsets.

Given the configuration of the SSFSE/HASTE sequences, it might seem that the inherent frequency distributions in the lung play a small, or secondary, role in the overall signal intensity through FA variations. However, the background gradients contribute to diffusion-related effects such that increased echo spacings lead to diminished lung parenchymal signal as reported by Ohno et al. (30). The diffusion dependence can be approximated by considering a constant gradient G applied throughout the SSFSE/HASTE acquisition which will then supplement the exponential T_2 decay through the relation:

$$S = So\, exp\,(-\gamma^2 G^2 \tau^3 \mathrm{D} n/12)\; exp\;(-R_2 n\tau) \quad [17]$$

where $n\tau$ is the nth echo time and D the diffusion, or pseudoperfusion, coefficient. Note the additional diffusion dependence of the decay on the cube of the echo spacing, indicating that shorter echo spacings reduce the effects of diffusion/perfusion. To date, truly quantitative studies of this effect are lacking, though the mechanism has been invoked and/or implicated in explaining T_2 measurement observations throughout the MR lung literature. It is interesting to examine what values for D and G, the two basic unknowns in Eq. [17], may offer a factor of ~35% reduction in signal at ETEs of ~40 ms when 5 ms vs. 2.5 ms echo spacings are employed, as in the study by Ohno et al. (30). Figure 10 shows two decay curves as calculated with Eq. [17] with echo spacings of 2.5 and 5 ms and an R_2 value of 25 s^{-1}, a D value of 10 microns^2/ms and a gradient term G of 8 Gauss/cm. One can note from these plots that at around 40 ms, the ETE employed by Ohno et al. (30), significant reduction of the signal with the larger echo spacing is observed.

STEADY STATE FREE PRECESSION SEQUENCES

Finally, we turn our attention to the class of sequences known generically as steady state free precession (SSFP) or balanced SSFP (bSSFP) sequences. Such sequences are now in common use for many clinical applications (58), particularly cardiac imaging (59), but have also been proposed as interesting candidates for fMRI studies (39,60), fast spectroscopic imaging (61), lung perfusion measurements (27), oxygen-enhanced lung imaging (62), and lung parenchymal signal intensity measurements in cystic fibrosis patients (18).

The bSSFP sequence consists of closely spaced RF pulses with flip angle θ separated by a repetition time τ and organized such that the imaging gradients employed are "balanced." Thus, in contrast to the spoiled gradient and SSFSE/HASTE sequences, the transverse magnetization is purposely retained rather than "spoiled" or "dephased," respectively, prior to each RF pulse. An interesting consequence of retaining the transverse magnetization in-phase, as Scheffler and Lehnhardt have noted (58), is that SSFP has "the highest possible signal-to-noise ratio (SNR) per unit time of all known sequences". Another consequence, however, is that the technique is quite sensitive to off-resonance effects with banding artifacts, e.g. severe loss of signal, occurring at specific frequencies at intervals associated with the inverse of the repetition time. Such bands may be observed in the bSSFP image in Fig. 11 (arrows) which shows the typical contrast characteristics of this sequence, often discussed as a T_2/T_1 type of contrast for common bSSFP imaging parameters (see Fig. 11 caption). It was not until scanners achieved gradient subsystems capable of generating gradient echo sequence fragments within τ periods on the order of ~6 ms or less to minimize the banding artifacts that bSSFP was able to make significant inroads in clinical practice.

A brief, and perhaps somewhat opinionated literature synopsis is posed in which three historical phases of bSSFP are recognized: The first phase is that from the early pioneers of the field including Carr (38) and Hinshaw (63), who used the Bloch equations to derive steady state magnetization components resulting from an infinite string of identical RF pulses. The second historical phase from the late 80s and early 90s includes the works of Gyngell (64) and Zur (65) who analyzed the bSSFP signal within the context of imaging sequences and considered the effects of static field inhomogeneities and fluid flow. Though fundamentally sound analyses were forwarded, explicit reference to reversible and irreversible effects were not made and the appendices provided in these works (64,65) are somewhat dense and difficult to absorb. Finally, the third historical phase of the current bSSFP literature employs rather unnecessarily complicated physical notions and obscure mathematics that are difficult to reproduce and/or utilize in simulations (66,67). Among these latter works is an assertion that the Lorentzian frequency distribution, discussed above and used very routinely in the field of magnetic resonance, yields "unphysical results" in bSSFP analyses (67), a statement with which we firmly disagree. The somewhat confusing literature on the topic in general has led to discussions as to whether bSSFP sequences were of a more spin echo or gradient echo character (68), a situation arguing for a more complete description based on the separation of reversible vs. irreversible transverse relaxation. As a consequence, some of us (69) recently extended the isochromat expressions for bSSFP magnetization, as provided in the first historical phase of bSSFP analyses (38,63), to incorporate the effects of intravoxel isochromat distributions $p(w)$ including the Lorentzian, Gaussian, and Uniform distributions of Eqs. [1] to [3]. We used the same methodology as provided in the analyses above, multiplying the isochromat signal intensity expressions by $p(w)$ and integrating over all w (69). Mathematical difficulties encountered were overcome by deploying a series expansion hitherto unnoted for this application with faster convergence properties than the double sum expansion discussed by Gyngell (64). The solution for the Gaussian and Uniform distributions still required numerical evaluation of a single infinite series but the Lorentzian distribution yielded a closed form solution similar to that derived by Ganter by more opaque means (67). The Lorentzian distribution solution is

provided in the appendix while the reader is referred to Ref. 69 for the solutions with Gaussian and Uniform distributions. The recently derived expressions were first applied to examine functional MRI mechanisms related to reversible vs. irreversible relaxation processes in the brain (69), while here we apply them to conditions suitable to the lung to explore how broad frequency distributions will affect bSSFP signal intensities.

Signal simulations for a bSSFP sequence with a τ value of 5 ms at the center of an echo readout at the mid-τ point (TE = 2.5 ms) are shown for lung parenchymal, nonparenchymal, and muscle tissues in the top row of Fig. 12 using the 1.5 T parameters provided in Table 1 for low (left) and high (right) FA values of 10° and 70°, respectively. The lower plots are magnitude simulations of the signal as a function of time t throughout the τ interval for the passband condition $w\tau = \pi$ for the same three tissues and FA values. Note that in these simulations the signals from the lung parenchyma have not been divided by 5 to account for the PD difference so as to better visualize the dependence on the bSSFP parameters themselves. Note that for the parenchymal lung components with a very high R_2' of 1,000 s^{-1}, exceedingly low signals from lung parenchyma are observed even in the passband (high signal) conditions at low and high FA values (top row, Fig. 12). Also the lower row demonstrates that moving the echoes closer to the RF pulses than usual, directly in the middle of the τ period, can yield significantly more signal. The recently derived expressions used for these simulations should prove more efficacious than direct numerical approaches as considered by Martirosian et al. in their studies of similar effects with bSSFP imaging of the lung at 1.5 T and 0.2 T field strengths (24), particularly with the closed form solution associated with the Lorentzian distribution.

CONCLUSIONS

Lung imaging with MRI is a currently active area of research and many aspects not covered in this work, including non-proton, hyperpolarized gas imaging of the lung, may be found in a recently published textbook, *MRI of the Lung* (70). We have attempted to outline how and why imaging lung parenchyma with proton MRI holds both promise and peril. We have outlined how the problems encountered, broad frequency distributions and low proton density, interact with the most common pulse sequences used for torso imaging. The detail we used to analyze the problem was quite extensive and, in some ways, novel. Namely, careful consideration of the separate contributions from reversible vs. irreversible transverse relaxation processes was provided, leading to detailed calculations that may help further optimize pulse sequences for proton MR studies of lung parenchyma and possibly greater use of this widespread modality for studies of the many diseases that affect lung structure and function. Ultimately we suspect that the complex and broad proton frequency distributions, or spectral patterns within lung parenchyma, may provide insights into lung microarchitecture and help elucidate various pathological states and perhaps be used to monitor the response to therapies for lung disorders.

Supplementary Material

Refer to Web version on PubMed Central for supplementary material.

Acknowledgments

This work was supported in part by the National Institute of Bio-medical Imaging And Bioengineering of the National Institutes of Health, Grant Number K01-EB015868.

APPENDIX

We used only three mathematical tools to perform the Bloch equation single isochromat analyses for each of the pulse sequence segments discussed above. These are two rotation matrices representing the effects of RF pulses along the *x*-axis and *y*-axis of the rotating frame. For in between these pulses, a free precession/relaxation matrix with the addition of a vector component to account for longitudinal spin-lattice relaxation was employed.

RF Pulses

The following two rotation matrices are used to represent the effects of RF pulses with flip angle θ along the *x*-axis and *y*-axis of the rotating frame:

$$\theta_x = \begin{matrix} 1 & 0 & 0 \\ 0 & cos\theta & sin\theta \\ 0 & -sin\theta & cos\theta \end{matrix} \quad \text{[A.1]}$$

$$\theta_y = \begin{matrix} cos\theta & 0 & sin\theta \\ 0 & 1 & 0 \\ -sin\theta & 0 & cos\theta \end{matrix} \quad \text{[A.2]}$$

Apologies to purists who like their rotations to have a strictly “positive” bent, because in the latter case the matrix represents a negative rotation about the *y*-axis. The free precession/relaxation (PR) plus longitudinal relaxation between pulses for time *t* are taken care of using:

$$PR = \begin{matrix} cos\ wt\ exp\,(-R_2 t) & sin\ wt\ exp\,(-R_2 t) & 0 \\ -sin\ wt\ exp\,(-R_2 t) & cos\ wt\ exp\,(-R_2 t) & 0 \\ 0 & 0 & exp\,(-R_1 t) \end{matrix} + \begin{matrix} 0 \\ 0 \\ m_{oo}(1 - exp\,(-R_1 t)) \end{matrix} \quad \text{[A.3]}$$

The elements of the vector **A** in Eq. [15] are given by

$$a_{11} = exp\,(-R_2\tau)\,[cos\theta\, cos^2(w\tau/2) - sin^2(w\tau/2)] \quad \text{[A.4a]}$$

$$a_{12} = exp\,(-R_2\tau)\ sin\,(w\tau/2)\ cos\,(w\tau/2)\ (1+cos\theta) \quad \text{[A.4b]}$$

$$a_{13} = exp\,(-(R_1+R_2)\tau/2)\ sin\theta\, cos\,(w\tau/2) \quad \text{[A.4c]}$$

$$a_{21} = -\,exp\,(-R_2\tau)\ sin\,(w\tau/2)\ cos\,(w\tau/2)\ (1+cos\theta) \quad \text{[A.4d]}$$

$$a_{22}=exp\,(-R_2\tau)[cos^2(w\tau/2)-cos\theta\,sin^2(w\tau/2)] \quad \text{[A.4e]}$$

$$a_{23}=-exp\,(-(R_1+R_2)\tau/2)sin\theta\,sin\,(w\tau/2) \quad \text{[A.4f]}$$

$$a_{31}=-exp\,(-(R_1+R_2)\tau/2)\,sin\theta\,cos\,(w\tau/2) \quad \text{[A.4g]}$$

$$a_{32}=-exp\,(-(R_1+R_2)\tau/2)\,sin\theta\,sin\,(w\tau/2) \quad \text{[A.4h]}$$

$$a_{33}=exp\,(-R_1\tau)\,cos\theta \quad \text{[A4.i]}$$

and the elements of the vector **B** in Eq. [15] are given by:

$$B_1=m_{oo}(1-exp\,(-R_1\tau/2))\\ exp\,(-R_2\tau/2)\,sin\theta\,cos(w\tau/2) \quad \text{[A.5a]}$$

$$B_2=-m_{oo}(1-exp\,(-R_1\tau/2))\\ exp\,(-R_2\tau/2)\,sin\theta\,sin\,(w\tau/2) \quad \text{[A.5b]}$$

$$B_3=m_{oo}(1-exp\,(-R_1\tau/2))\,[1+cos\theta\,exp\,(-R_1\tau/2)] \quad \text{[A.5c]}$$

SSFP Lorentzian Distribution Solution

The steady state transverse magnetization or signal during time *t* for a string of θ_x pulses separated by inversion time τ and for a single isochromat *w* is given by the following expression (38):

$$S(t)=(c/a)\,\{exp\,(-iwt)\,exp\,(-R_2t)\\ -exp\,(iw(\tau-t)\,exp\,(-R_2(\tau+t)\}\;/[1-(b/a)\,cos\,(w\tau)] \quad \text{[A.6]}$$

with

$$a\equiv 1-exp\,(-(R_1+2R_2)\tau)\\ -cos\theta\,[exp\,(-R_1\tau)-exp\,(-2R_2\tau)] \quad \text{[A.7a]}$$

$$b\equiv(1+cos\theta)\,exp\,(-R_2\tau)\,[1-exp\,(-R_1\tau)] \quad \text{[A.7b]}$$

$$c\equiv im_{oo}sin\theta[1-exp\,(-R_1\tau)]. \quad \text{[A.7c]}$$

Multiplying Eq. [A.6] by the Lorentzian distribution of Eq. [1] and integrating over all real *w* leads to the following closed form expression (69) for calculating the signal as a function of the linewidth and central frequency parameters R_2' and w_o of the distribution:

$$S_{Lor}(t) = FID_{Lor} - ECHO_{Lor} \quad \text{[A.8a]}$$

where

$$\begin{gathered} FID_{Lor} = (c/ag)\, exp(-iw_o t) \\ \{exp - ((R_2 + R_2')t)\ \{h/[h - (1-g)\, exp(-(iw_o + R_2')\tau)]\} \\ + (c/ag)\, exp(-iw_o t)\, exp(-R_2 - R_2')t) \\ \{(1-g)/[h\, exp(-(iw_o - R_2')\tau) - 1 + g]\} \end{gathered} \quad \text{[A.8b]}$$

and

$$\begin{gathered} Echo_{Lor} = (c/ag)\, exp(iw_o(\tau - t))\, exp(-(R_2 + R_2')\tau) \\ exp(-(R_2 + R_2')t)\, \{h/[h - (1-g)\, exp((iw_o - R_2')\tau)]\} \\ + (c/ag)\, exp(iw_o(\tau - t))\, exp(-(R_2 - R_2')\tau) \\ exp(-(R_2 + R_2')t)\, \{(1-g)/[h\, exp((iw_o + R_2')\tau) - 1 + g]\} \end{gathered} \quad \text{[A.8c]}$$

where $h = b/a$ and $g = (1 - h^2)^{1/2}$.

References

1. Ailion DC, Case TA, Blatter D, Morris AH, Cutillo AG, Durney CH, et al. Application of NMR spin imaging to the study of lungs. Bull Magn Reson. 1984; 6:130–139.
2. Case TA, Durney CH, Ailion DC, Cutillo AG, Morris AH. A mathematical model of diamagnetic line broadening in lung tissue and similar heterogeneous systems: calculations and measurements. J Magn Reson. 1987; 73:304–314.
3. Kveder M, Zupancic I, Lahajnar G, Blinc R, Suput D, Ailion DC, et al. Water proton NMR relaxation times in tissue. Magn Reson Med. 1988; 7:432–441. [PubMed: 3173058]
4. Durney CH, Bertolina JA, Ailion DC, Christman R, Cutillo AG, Hashemi S. Calculation and interpreation of inhomogeneous line broadening in models of lung and other heterogeneous structures. J Magn Reson. 1989; 85:554–570.
5. Bertolina JA, Durney CH, Ailion DC, Cutillo AG, Morris AH, Goodrich KC. Experimental verification of inhomogeneous line-broadening calculations in lung models and other inhomogeneous structures. J Magn Reson. 1992; 99:161–169.
6. Ailion DC. Potential industrial applications of inhomogeneous broadening imaging. Magn Reson Imaging. 1992; 10:799–808. [PubMed: 1461075]
7. Christman RA, Ailion DC, Case TA, Durney CH, Cutillo AG, Shioya S, et al. Comparison of calculated and experimental NMR spectral broadening for lung tissue. Magn Reson Med. 1996; 5:6–13. [PubMed: 8771017]
8. Cutillo, AG., editor. Application of Magnetic Resonance in the Study of Lung. Armonk, NY: Futura Publishing Company Inc; 1996.
9. Jackson, JD., editor. Classical Electrodynamics. 2. New York NY: John Wiley and Sons; 1975. Magnetostatics.
10. Griffiths, DJ. Introduction to Electrodynamics. 3. Upper Saddle River, NJ: Prentice Hall; 1981.
11. Gold GE, Pauly JM, Leung AN, Block WF, Meyer CH, Sze R, et al. Short echo time spectroscopic imaging of the lung parenchyma. J Magn Reson Imaging. 2002; 15:670–684.
12. Bergin CJ, Glover GH, Pauly JM. Lung parenchyma: magnetic susceptibility in MR imaging. Radiology. 1991; 180:845–848. [PubMed: 1871305]
13. Bergin CJ, Noll DC, Pauly JM, Glover GH, Macovski A. MR imaging of lung parenchyma: a solution to susceptibility. Radiology. 1992; 183:673–676. [PubMed: 1584917]
14. Bergin CJ, Pauly JM, Macovski A. Lung parenchyma: projection reconstruction MR imaging. Radiology. 1991; 179:777–781. [PubMed: 2027991]

15. Wild JM, Marshall H, Bock M, Schad LR, Jakob PM, Puderbach M, et al. MRI of the lung (1/3): methods. Insights Imaging. 2012; 3:345–53. [PubMed: 22695952]
16. Alsop DC, Hatabu H, Bonnet M, Listerud J, Gefter W. Multi-slice, breathhold imaging of the lung with submillisecond echo times. Magn Reson Med. 1995; 33:678–682. [PubMed: 7596272]
17. Hatabu H, Gaa J, Tadamura E, Edinburgh KJ, Stock KW, Garpestad E, et al. MR imaging of pulmonary parenchyma with a half-Fourier single-shot turbo spin-echo (HASTE) sequence. Eur J Radiol. 1999; 29:152–159. [PubMed: 10374663]
18. Failo R, Wielopolski PA, Tiddens AWM, Hop WCJ, Mucelli RP, Lequin MH. Lung morphology assessment using MRI: A robust ultra-short TR/TE 2D steady state free precession sequence used in cystic fibrosis patients. Magn Reson Med. 2009; 1:299–306. [PubMed: 19165879]
19. Hatabu H, Alsop DC, Listerud J, Bonnet M, Gefter WB. T_2* and proton density measurement of normal human lung parenchyma using submillisecond echo time gradient echo magnetic resonance imaging. Eur J Radiol. 1999; 9:245–252. [PubMed: 10399610]
20. Stock KW, Chen Q, Hatabu H, Edelman RR. Magnetic resonance T_2* measurements of the normal lung in vivo with ultra-short echo times. Magn Reson Imaging. 1999; 7:997–1000. [PubMed: 10463650]
21. Theilmann RJ, Arai TJ, Samiee A, Dubowitz DJ, Hopkins SR, Buxton RB, et al. Quantitative MRI measurement of lung density must account for the change in T_2* with lung inflation. J Magn Reson Imaging. 2009; 0:527–534. [PubMed: 19630079]
22. Ohno Y, Koyama H, Yoshikawa T, Matsumoto K, Takahashi M, Cauteren MV, et al. T_2* measurements of 3-T MRI with ultrashort TEs: Capabilities of pulmonary function assessment and clinical stage classification in smokers. AJR Am J Roentgenol. 2011; 97:W279–W285. [PubMed: 21785054]
23. Yu J, Xue Y, Song HK. Comparison of lung T_2* during free-breathing at 1.5 T and 3.0 T with ultrashort echo time imaging. Magn Reson Med. 2011; 6:248–254. [PubMed: 21695727]
24. Martirosian P, Boss A, Fenchel M, Deimling M, Schafer J, Claussen CD, et al. Quantitative lung perfusion mapping at 0.2 T using FAIR True-FISP MRI. Magn Reson Med. 2006; 55:1065–1074. [PubMed: 16602073]
25. Johnson KM, Fain SB, Schiebler ML, Nagle S. Optimized 3D ultrashort echo time pulmonary MRI. Magn Reson Med. 2013; 70:1241–1250. [PubMed: 23213020]
26. Mayo JR, Mackay A, Muller NL. MR imaging of the lungs: value of short TE spin-echo pulse sequences. AJR Am J Roentgenol. 1992; 159:951–956. [PubMed: 1414805]
27. Estilaei M, MacKay A, Whittall K, Mayo J. In vitro measurement of water content and T_2 relaxation times in lung using a clinical MRI scanner. J Magn Reson Imaging. 1999:699–703. [PubMed: 10331766]
28. Shioya S, Christman R, Ailion DC. An in vivo determination of multiexponential Hahn T_2 of normal lung. Magn Reson Med. 1990; 16:49–56. [PubMed: 2255237]
29. Cutillo AG, Chan PH, Ailion DC, Watanabe S, Rao NV, Hansen CB, et al. Characterization of bleomycin lung injury by nuclear magnetic resonance: correlation between NMR relaxation and lung water and collagen content. Magn Reson Med. 2002; 47:246–256. [PubMed: 11810667]
30. Ohno Y, Oshio K, Uematsu H, Nakatsu M, Gefter WB, Hatabu H. Single-shot half-Fourier RARE sequence with ultra-short inter-echo spacing for lung imaging. J Magn Reson Imaging. 2004; 20:336–339. [PubMed: 15269963]
31. Edelman RR, Hatabu H, Tadamura E, Li W, Prasad PV. Noninvasive assessment of regional ventilation in the human lung using oxygen enhanced magnetic resonance imaging. Nature Med. 1996:1236–1239. [PubMed: 8898751]
32. Stock KW, Chen Q, Morrin M, Hatabu H, Edelman RR. Oxygen enhanced magnetic resonance ventilation imaging of the human lung at 0.2 T and 1.5 T. J Magn Reson Imaging. 1999; 9:839–841.
33. Mai VM, Knight-Scott J, Berr SS. Improved visualization of the human lung in 1H MRI using multiple inversion recovery for simultaneous suppression of signal contributions from fat and muscle. Magn Reson Med. 1999; 41:866–870. [PubMed: 10332866]
34. Iwasawa T, Takahashi H, Ogura T, Asakura A, Gotoh T, Kagei S, et al. Correlation of lung parenchymal MR signal intensity with pulmonary function tests and quantitative computed

tomography (CT) evaluation: a pilot study. J Magn Reson Imaging. 2007; 26:1530–1536. [PubMed: 17968893]

35. Holverda S, Theilmann RJ, Rui C, Arai TJ, Hall ET, Dubowitz DJ, et al. Measuring lung water: ex vivo validation of multi-image gradient echo MRI. J Magn Reson Imaging. 2011; 34:220–224. [PubMed: 21698711]
36. Bankier AA, Storey P, Mai VM, Edelman RR, Chen Q. Gravity-dependent signal gradients on MR images of the lung in supine and prone positions: a comparison with isogravitational signal variability. J Magn Reson Imaging. 2006; 23:115–122. [PubMed: 16400636]
37. Azzalini A. A class of distributions which includes the normal ones. Scand J Statist. 1985; 12:171–178.
38. Carr HV. Steady-state free precession in nuclear magnetic resonance. Phys Rev. 1958; 112:1693–1701.
39. Lee JH, Dumoulin SO, Saritas EU, Glover GH, Wandell BA, Nishimura DG, et al. Full brain coverage and high-resolution imaging capabilities of passband b-SSFP fMRI at 3 T. Magn Reson Med. 2008; 59:1099–1110. [PubMed: 18421687]
40. Marsden, JE. Basic Complex Analysis. San Francisco, CA: Freeman; 1973.
41. Gradshteyn, IS.; Ryzhik, IM. Table of Integrals, Series, and Products. 7. Burlington, MA: Academic Press; 2007.
42. Ma J, Wehrli FW. Method for image-based measurement of the reversible and irreversible contribution to the transverse-relaxation rate. J Magn Reson B. 1996; 111:61–69. [PubMed: 8620286]
43. Mulkern RV, Williams ML. The general solution to the Bloch equation with constant RF and relaxation terms Application to saturation and slice selection. Med Phys. 1993; 20:5–13. [PubMed: 8455512]
44. Mulkern RV. In-plane spatial encoding in MRI and its central role in determining contrast and artifact with RF echo planar techniques. Conc Magn Reson. 1992; 4:307–325.
45. Margosian P, Schmitt F, Purdy D. Faster MR imaging: imaging with half the data. Health Care Instrum. 1986; 1:195–197.
46. Feinberg DA, Hale JD, Watts JC, et al. Halving MR imaging time by conjugation: demonstration at 3.5 kG. Radiology. 1986; 161:527–531. [PubMed: 3763926]
47. Mulkern RV, Wong STS, Winalski C, Jolesz FA. Contrast manipulation and artifact assessment of 2D and 3D RARE sequences. Magn Reson Imaging. 1990; 8:557–566. [PubMed: 2082125]
48. Mulkern RV, Melki PS, Jacob P, Higuchi N, Jolesz FA. Phase encode order and its effect on contrast and artifact in single-shot RARE sequences. Med Phys. 1991; 18:1032–1037. [PubMed: 1961143]
49. Melki PS, Jolesz FA, Mulkern RV. Partial RF echo planar imaging with the FAISE method: I. Experimental and theoretical assessment of artifact. Magn Reson Med. 1992; 26:328–341. [PubMed: 1513254]
50. Melki PS, Jolesz FA, Mulkern RV. Partial RF echo planar imaging with the FAISE method. II. Contrast equivalence with spin echo sequences. Magn Reson Med. 1992; 26:342–354. [PubMed: 1513255]
51. Constable RT, Anderson AW, Zhong J, Gore JC. Factors influencing contrast in fast spin-echo imaging. Magn Reson Imaging. 1992; 10:497–511. [PubMed: 1501520]
52. Chien D, Mulkern RV. Fast spin-echo studies of contrast and small lesion definition using a liver-metastasis model. J Magn Reson Imaging. 1992; 2:483–487. [PubMed: 1633403]
53. Henzler T, Dietrich O, Krissak R, Wichmann T, Lanz T, Reiser MF, et al. Half-Fourier-acquisition single-shot turbo spin-echo (HASTE) MRI of the lung at 3 Tesla using parallel imaging with 32-receiver channel technology. J Magn Reson Imaging. 2009; 30:541–546. [PubMed: 19711408]
54. Heidemann RM, Griswold MA, Kiefer B, et al. Resolution enhancement in lung 1H imaging using parallel imaging methods. Magn Reson Med. 2003; 49:391–394. [PubMed: 12541262]
55. Mugler JP III, Bao S, Mulkern RV, Guttmann CR, Robertson RL, Jolesz FA, et al. Optimized single-slab three-dimensional spin-echo MR imaging of the brain. Radiology. 2000; 216:891–899. [PubMed: 10966728]

56. Busse RF, Hariharan H, Vu A, Brittain JH. Fast spin echo sequences with very long echo trains: design of variable refocusing flip angle schedules and generation of clinical T_2 contrast. Magn Reson Med. 2006; 55:1030–1037. [PubMed: 16598719]
57. Meiboom S, Gill D. Modified spin-echo method for measuring nuclear relaxation times. Rev Sci Inst. 1958; 29:688–691.
58. Scheffler K, Lehnhardt S. Principles and applications of balanced SSFP techniques. Eur Radiol. 2003; 13:2409–2418. [PubMed: 12928954]
59. Mulkern RV, Chung T. From signal to image: magnetic resonance imaging physics for cardiac magnetic resonance. Pediatr Cardiol. 2000; 21:5–17. [PubMed: 10672610]
60. Zhong K, Leupold J, Hennig J, Speck O. Systematic investigation of balanced steady-state free precession for functional MRI in the human visual cortex at 3 Tesla. Magn Reson Med. 2007; 57:67–73. [PubMed: 17191247]
61. Speck O, Scheffler K, Hennig J. Fast 31P chemical shift imaging using SSFP methods. Magn Reson Med. 2002; 48:633–639. [PubMed: 12353280]
62. Muller CJ, Loffler R, Deimling M, Peller M, Reiser M. MR lung imaging at 0.2 T with T_1-weighted true FISP:Native and oxygen-enhanced. J Magn Reson Imaging. 2001; 14:164–168. [PubMed: 11477675]
63. Hinshaw WS. Image formation by nuclear magnetic resonance: the sensitive-point method. JAppl Phys. 1976; 47:3709–3721.
64. Gyngell ML. The steady-state signals in short-repetition time sequences. J Magn Reson. 1989; 81:474–483.
65. Zur Y, Stokar S, Bendel P. An analysis of fast imaging sequences with steady-state transverse magnetization refocusing. Magn Reson Med. 1988; 6:175–193. [PubMed: 3367775]
66. Hanicke W, Vogel HU. An analytical solution for the SSFP signal in MRI. Magn Reson Med. 2003; 49:771–775. [PubMed: 12652550]
67. Ganter C. Static susceptibility effects in balanced SSFP sequences. Magn Reson Med. 2006; 56:687–691. [PubMed: 16826609]
68. Scheffler K, Hennig J. Is TrueFisp a gradient-echo or a spin-echo sequence? Magn Reson Med. 2003; 49:395–397. [PubMed: 12541263]
69. Mulkern RV, Balasubramanian M, Orbach DB, Mitsouras D, Haker SJ. Incorporating reversible and irreversible transverse relaxation effects into steady state free precession (SSFP) signal intensity expressions for fMRI considerations. Magn Reson Imaging. 2013; 31:346–352. [PubMed: 23337079]
70. Kauczor, HU.; Altes, TA., editors. MRI of the Lung. Berlin: Springer; 2009.

Biographies

Robert V. Mulkern received his PhD in physics from Brown University in 1986 where his thesis was devoted to solid state nuclear magnetic resonance studies of glass under the guidance of the late Professor Philip J. Bray. Dr Mulkern then lectured for a year at the University of Rhode Island followed by entry into the then burgeoning field of magnetic resonance imaging (MRI), as practiced in the context of diagnostic radiology. Beginning with a postdoctoral fellowship at the Brigham and Women's Hospital, an affiliate of Harvard Medical School (HMS), Dr Mulkern received his primary and current appointment

in the faculty of the Radiology department at Children's Hospital, Boston, MA, also an affiliate of HMS, and currently serves as the scientific director of the MRI division. He has had longstanding academic and research interests in determining just what the nuclear magnetic resonance signal from tissue really means. In pursuit of this interest he has contributed to the development and application of fast imaging and fast spectroscopic imaging methods. He has also provided quantum mechanical calculations of coupled spin-system spectra as acquired with typical multi-pulse localization schemes, performed detailed tissue relaxation studies and demonstrated multi-component tissue water diffusion decay curves in brain and prostate. In the present work, the rather unique tissue relaxation properties of lung parenchyma are reviewed and placed within the context of modern thoracic MR imaging, a feat which includes the development and expose of analyses suitable for separating reversible from irreversible transverse relaxation, a focus of more recent interest for Dr Mulkern and, to date, an area largely underappreciated by most practitioners of MRI.

Hatsuho Mamata, MD, PhD, is a general neuroradiologist. She graduated from the Tokai University School of Medicine, Kanagawa, Japan in 1989. She completed her Radiology residency and fellowship in Tokai University Hospital in 1994. She joined the Department of Radiology, Tokai University Hospital as an instructor. While she was there, she participated in clinical research and presented her results at International Society for Magnetic Resonance in Medicine as well as European Congress of Radiology. She received a PhD in medical science from Tokai University in 2001. She joined the MRI division, Radiology at Brigham and Women's Hospital as a research fellow in 1998. Her major interest at the Brigham was Diffusion-weighted imaging (especially Line Scan Diffusion) and Perfusion imaging of the brain and spinal cord, and more recently lung cancer and parathyroid adenomas. Her educational exhibit for mesothelioma received Cum Laude Award from the Radiological Society of North America in 2010. She was granted instructor of Radiology in 2003, and assistant professor of Radiology in 2006 from Harvard Medical School. She obtained a US medical license in 2009, completed clinical MRI fellowship in 2010, and an Image Guided Therapy fellowship in 2013 both at the Brigham and Women's Hospital. She continued to participate in a Neuroradiology fellowship at the University of North Carolina hospitals and completed the program in June, 2014. Her representative research in perfusion of pulmonary nodules was published in Magnetic Resonance in Medicine (Magn Reson Med. 2012 Nov;68(5): 1614-22).

Dimitris Mitsouras received his ScB in Computer Science from Brown University in 1998 and his PhD in Electrical Engineering and Computer Science from MIT in 2004. His dissertation developed non-Fourier MRI encoding techniques by casting the imaging of a sample using selective excitations as a matrix-vector multiplication. Dr. Mitsouras joined the Brigham And Women's Hospital and Harvard Medical School in 2004 as an Instructor in Radiology, where he remains to-date as Assistant Professor of Radiology. He is the Director of MRI Research and Medical Physics at the Applied Imaging Science Lab at BWH. Dr. Mitsouras research interests span all aspects of cardiovascular MR and CT imaging that fall under the purview of his multi-disciplinary training in computational physics. He has made several contributions to the field of MRI, including a dual-echo spacing fast spin echo technique to accommodate volume selection in conjunction with non-selectively refocused echo trains, an approach now used in e.g., the 3D SPACE sequence on the Siemens MRI platform; and a computationally tractable algorithm for the exact Fourier inversion of k-space samples acquired with rotationally symmetric non-Cartesian patterns, such as multi-shot spirals. He is currently funded by an NIH Career Development Award from the NIBIB to pursue a novel approach for extracting quantitative blood flow from contrast-enhanced CT angiography, with the goal of non-invasive detection of functionally significant coronary artery disease.

Mukund Balasubramanian received his BS in physics from the University of Texas at Austin and his PhD in computational neuroscience from Boston University in 2006. Dr Balasubramanian joined Boston Children's Hospital as a postdoctoral fellow in 2010 and is currently an Instructor in the Department of Radiology. He has a broad interdisciplinary background, with research contributions in areas such as computational geometry, image processing and segmentation, mathematical modeling of topographic maps in the brain and functional neuroimaging. His more recent research interests are in the development of improved MRI pulse sequences and analysis techniques for imaging brain structure and function, and in investigating the possibility that some of these methods may also prove useful in the study of other tissues such as lung parenchyma or bone marrow.

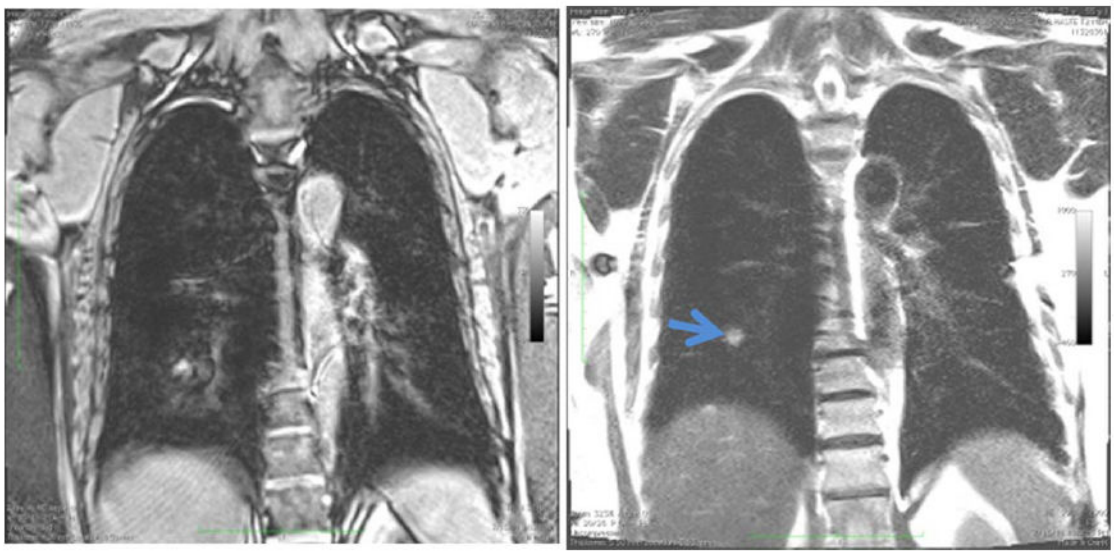

Figure 1.

Large FOV coronal images of a patient with lung cancer acquired with gradient echo (left) and spin echo (right)-based images, both within breathholds and in multislice formats. These images were acquired at 3 T with a Siemens scanner (Erlangen, Germany) using (left) a three-dimensional volume interpolated breathhold (VIBE) spoiled gradient echo imaging sequence with a TR/TE = 3.4/1.3 ms, ±250 kHz receiver bandwidth, 4 mm slice thickness with in-plane voxel dimensions of 1.25 × 1.54 mm^2 and (right) with an SSFSE/HASTE sequence with a TR/TE = 1,200/100 ms, ±390 kHz receiver bandwidth, 5.5 mm slice thickness with in-plane voxel dimensions of 1.25 × 1.25 mm^2. The 1.3 ms TE of the gradient echo image results in fat and water being out-of-phase at 3 T, causing characteristic shading of border regions between fat and water. Furthermore, the VIBE images were acquired post-gadolinium contrast administration, resulting in bright blood in the aorta due to shortened blood T_1. Aortic blood is dark in the SSFSE sequence as blood exits the two-dimensional coronal plane within the 100 ms window provided by the ETE of 100 ms. The tumor appears bright in both images (arrow in SSFSE image) due to increased water accumulation in SSFSE and Gd uptake in VIBE, bright within the void of lung parenchyma provided by both sequences. The actual signal intensity values within lung parenchyma regions without obvious blood vessels is similar to values for noise measured in air outside of the body, primarily phase encoding ghost noise, in both sequences.

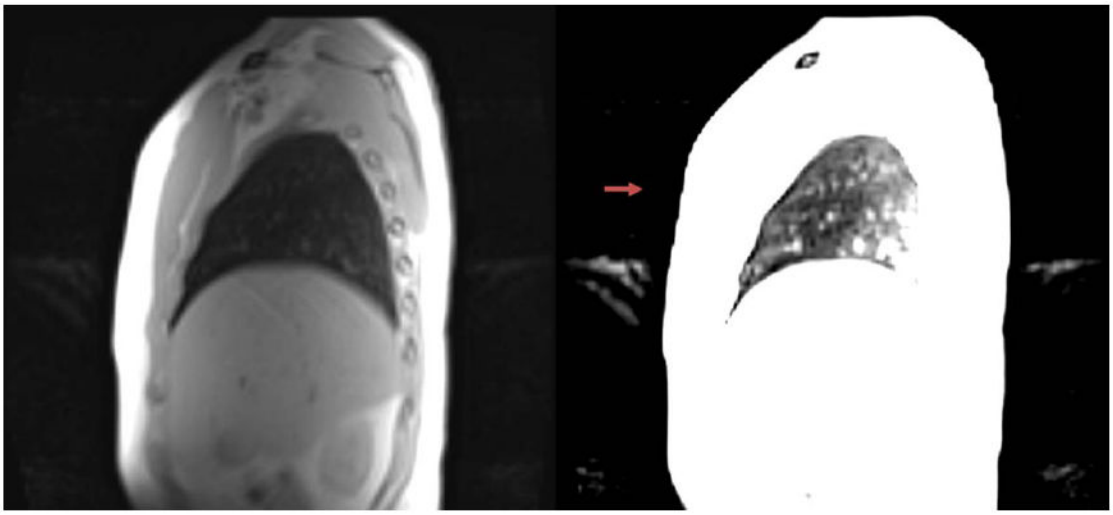

Figure 2.

Sagittal images of a healthy volunteer demonstrating that signal can be extracted from the void of lung parenchyma. The images were acquired on a 1.5-T Siemens scanner (Erlangen, Germany) with a single spin echo two-dimensional-FT imaging sequence using a short TE of 3.7 ms and a long TR of 3 s. Other parameters were a 5 mm slice thickness with a 3 × 3 mm^2 in-plane resolution and a 6.4 min scan time during shallow breathing. Signal intensities within lung parenchyma within regions showing no obvious blood vessels were 7 to 10 times higher than noise levels at the level of the arrow shown in the right hand figure where ghosting artifact was minimal. The lung parenchymal signal values were, however, some 5 and 12 times smaller than muscle and fat signal intensities, respectively. The factor of 5 compared with muscle is consistent with the reduced proton density in lung parenchyma. Note the increased lung parenchymal signal in the posterior region of the lung which is consistent with a gravitational pooling of water in this supine position.

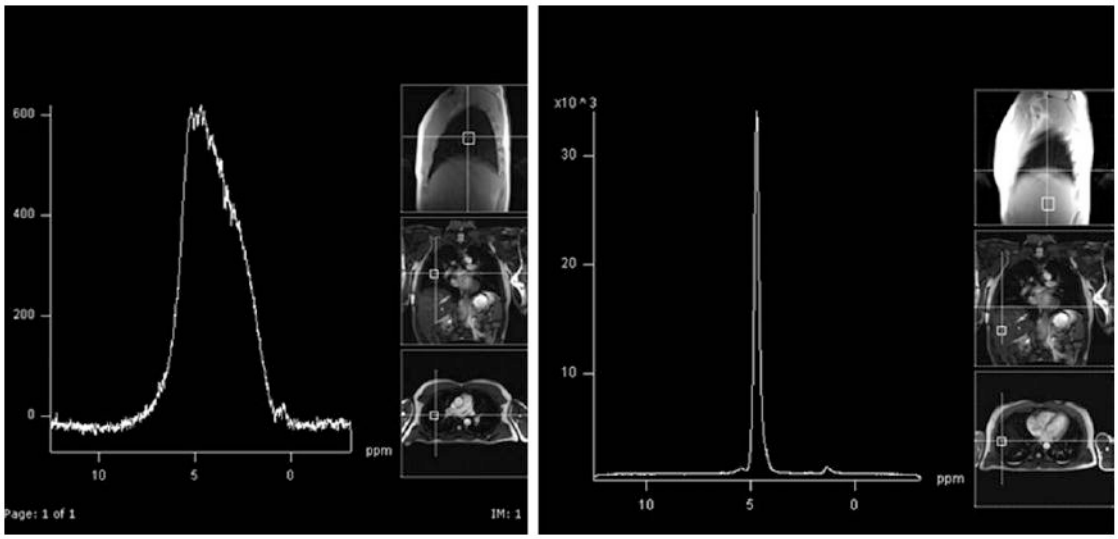

Figure 3.

Single voxel (2.5 cm^3) spectra from lung (left) and liver (right) at 1.5 T of a healthy volunteer as acquired with a PRESS acquisition using a TR of 3 s, 32 signal averages, and a TE of 30 ms. The lung spectrum is asymmetric and extremely broad with a full width at half-height of approximately 6 ppm or 390 Hz. The water resonance in the liver has a full width at half-height of less than 0.3 ppm or 35 Hz.

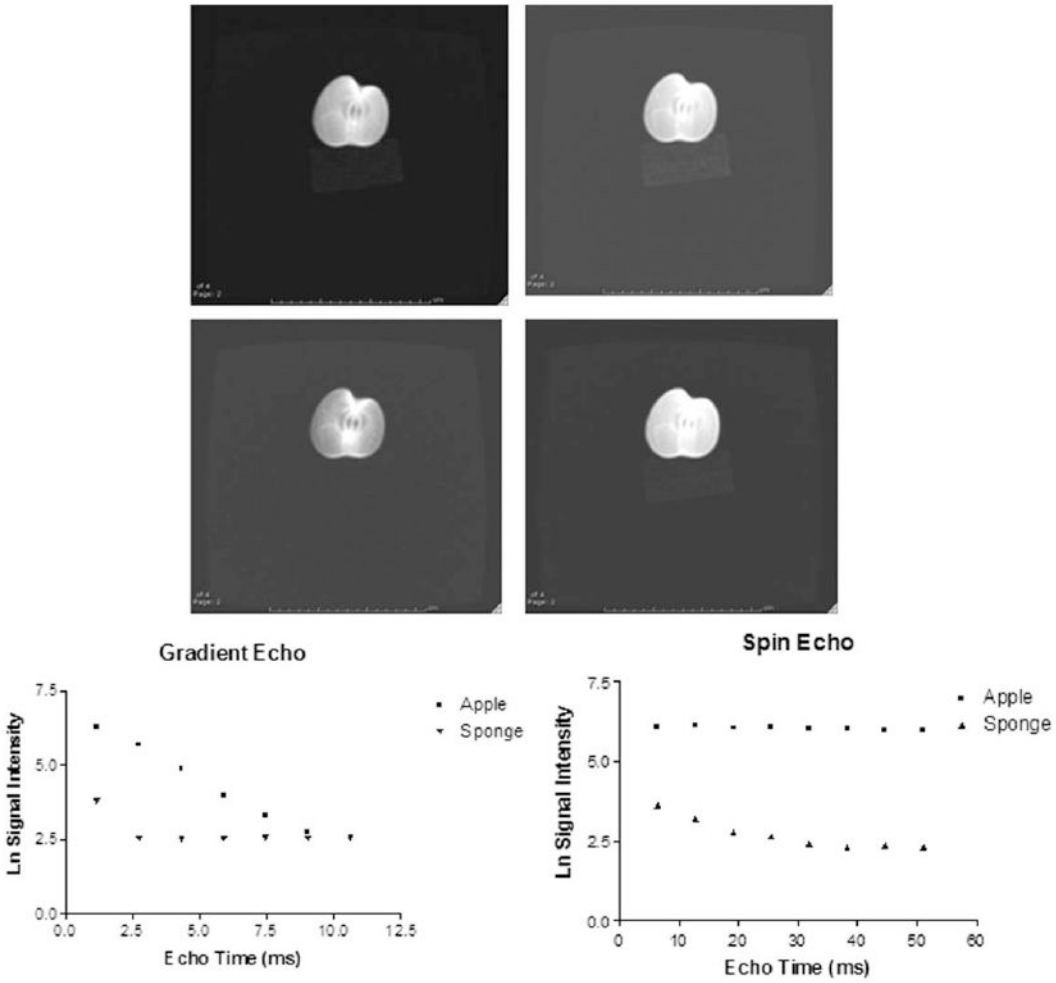

Figure 4.

Images of an apple sitting on top of a sponge packet (windowed for optimal viewing of the sponge, top) as acquired with a 1.5-T scanner (General Electric Medical systems, Milwaukee WI). The sponge material is contained within the original, unopened cellophane wrappers in which it was purchased ("Utility Sponge," Foodhold USA, LLC, Landover, MD) and so contains only residual moisture. The images on the left are the first two of eight gradient echo images acquired with an initial TE of 1.2 ms followed by images acquired every 1.5 ms with the second image at TE = 2.7 ms showing no signal from the sponge. The images on the right are the first two of eight spin echo images acquired with a CPMG sequence which is the skeletal basis of FSE/TSE and SSFSE/HASTE imaging and within which the sponge is clearly visible in both 1st, 2nd, and even subsequent spin echo images (not shown) acquired with TEs of 6.4 ms and 12.7 ms, respectively, and every 6.4 ms intervals thereafter. T_2* (bottom left) and T_2 (bottom right) decay curves (Ln signal intensity vs. TE) from 2 cm^2 ROI's within the apple and sponge from the gradient echo train and CPMG train, respectively. Note how the sponge signal plunges into the noise floor after a single gradient echo (T_2* < 1.2 ms), yet remains above the noise floor for at least 4 spin echoes (a TE around 25 ms) with a T_2 value of approximately 21 ms. The apple also has a short T_2* of 2.1 ms while its T_2 value is calculated to be around 310 ms. Both of these

objects have transverse relaxation properties similar to lung parenchyma due to the air within them, with the sponge more like lung due to its very low proton density.

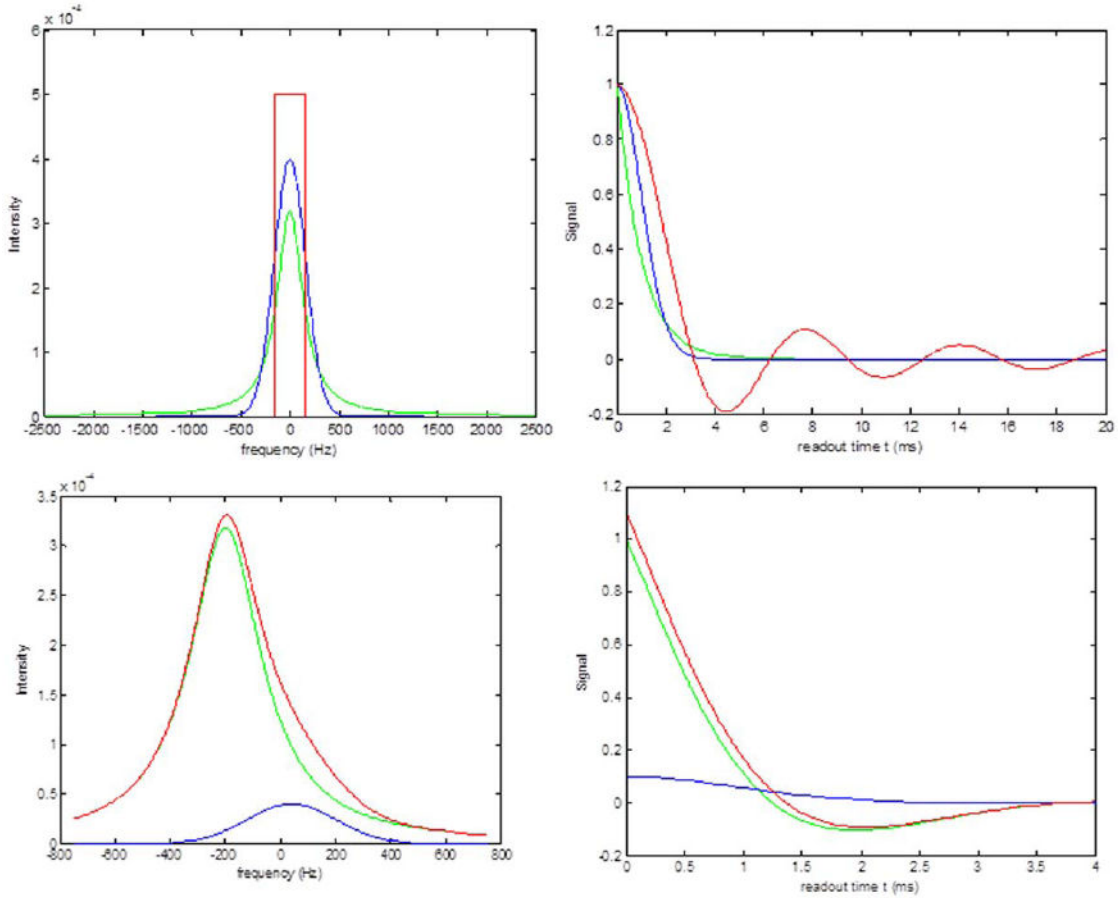

Figure 5.

The three frequency distributions (upper left) defined in the text: Lorentzian (green), Gaussian (blue), and Uniform (red), all with the relatively broad nominal width parameters R_2', σ, and Δ of 1,000 Hz, leading to short time domain signal decays in lung parenchyma. The three simulated time domain FID signals (real part) associated with the three distributions (upper right) were calculated using an R_2 value of 25 s^{-1}. Note that only for the green curve generated from the Lorentzian distribution is the time domain signal a pure monoexponential decay while the red curve from the Uniform distribution demonstrates oscillations associated with the sinc function. The blue curve generated from the Gaussian distribution is, in fact, a Gaussian. A simulation of a 1.5 T lung parenchymal spectrum (lower left) modeled as the sum (red) of an underlying Lorentzian distribution (green) and a Gaussian distribution (blue) 1/10 as large. The two distributions are separated by 240 Hz in this model and both have linewidth parameters R_2' and σ of 1,000 s^{-1}. The red spectrum demonstrates asymmetry associated with the line shapes calculated by Christman et al. (Ref. 7, Fig. 4) using the WS foam model and to that seen in the experimental spectrum of Fig. 3. Having an analytic estimate of the asymmetric spectrum, however, allows for explicit calculation of the time domain signals (lower right) that would be acquired following excitation and assuming a 25 s^{-1} value for the irreversible relaxation rate R_2.

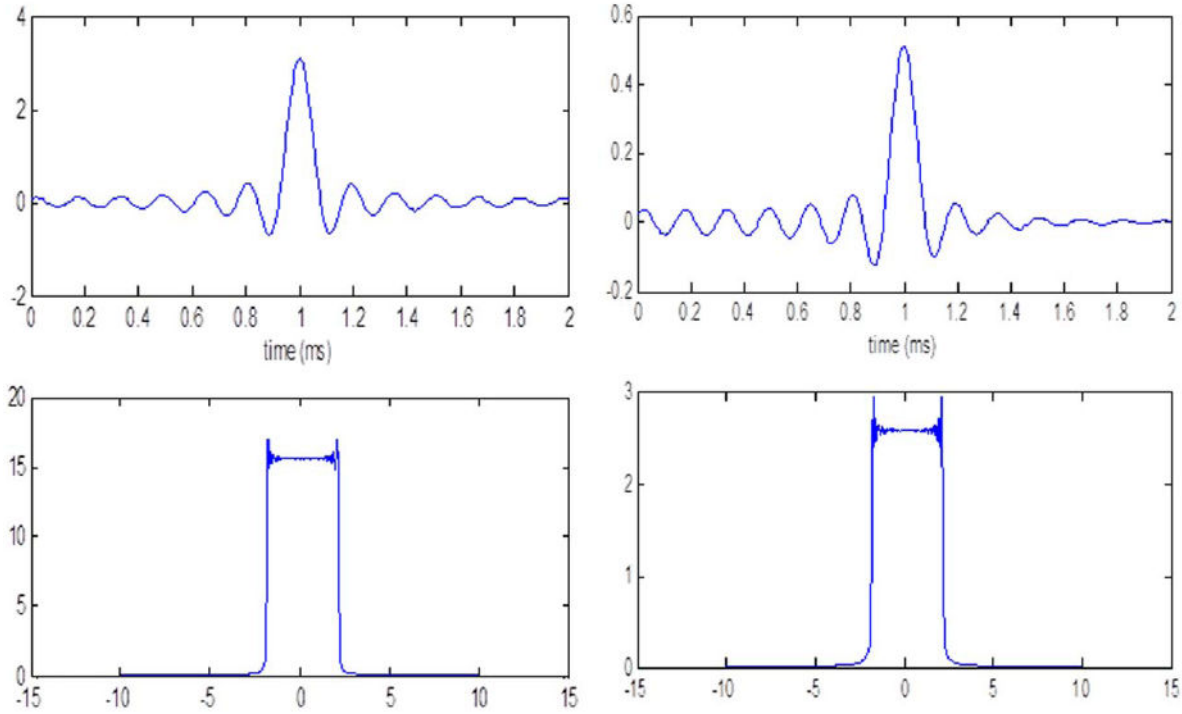

Figure 6.

Gradient echoes (top) collected in the presence of a readout gradient of 1.5 Gauss/cm (15 mT/m) and a TE of 2 ms for nonparenchymal lung tissue (left) with an R_2' of 100 s^{-1} and parenchymal lung components (right) with R_2' of 1,000 s^{-1}. Note the diminished signal by nearly a factor of 10 in the parenchymal echo signal and the greater asymmetry of this echo. Projections reconstructed from Fourier transforming these echoes (bottom) show similar decrease of signal in the parenchymal vs. nonparenchymal components as well as significantly larger edge artifact, ~15% of mean vs. ~5% of mean signal, in the parenchymal projection.

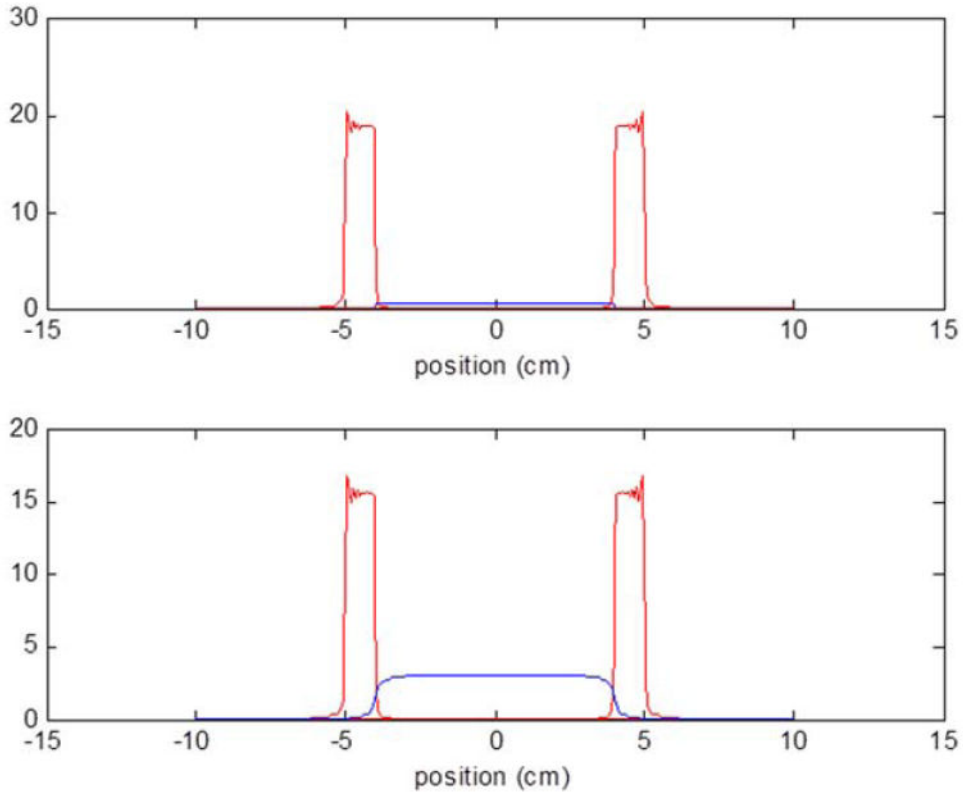

Figure 7.

Simulated torso projection from a gradient echo (top) vs. spin echo (bottom) acquisitions with respective TE values of 2 and 10 ms. The simulations were generated assuming lung parenchyma (blue) from −4 to 4 cm sandwiched by 1 cm muscle tissue slabs at 4.5 and −4.5 cm locations and with lung signal divided by 5 to account for the reduced proton density. R_2 values for both tissues were set at 25 s^{-1} while lung parenchyma was assumed to have an R_2' of 1,000 s^{-1} and muscle an R_2' of 5 s^{-1}. Readout gradient strengths for the gradient echo were 1.5 Gauss/cm (15 mT/m) and 0.3 Gauss/cm (3 mT/m) for the spin echo with 256 sampling points used for each. The full bandwidths for gradient echo and spin-echo simulations were ±64,000 Hz and ±12,800 Hz, respectively, or equivalently, ±250 Hz/voxel and ±50 Hz/voxel. Despite the factor of 5 longer echo time for the spin echo simulation, the 180° refocusing pulse restored a substantial amount of lung signal compared to the gradient echo acquisition.

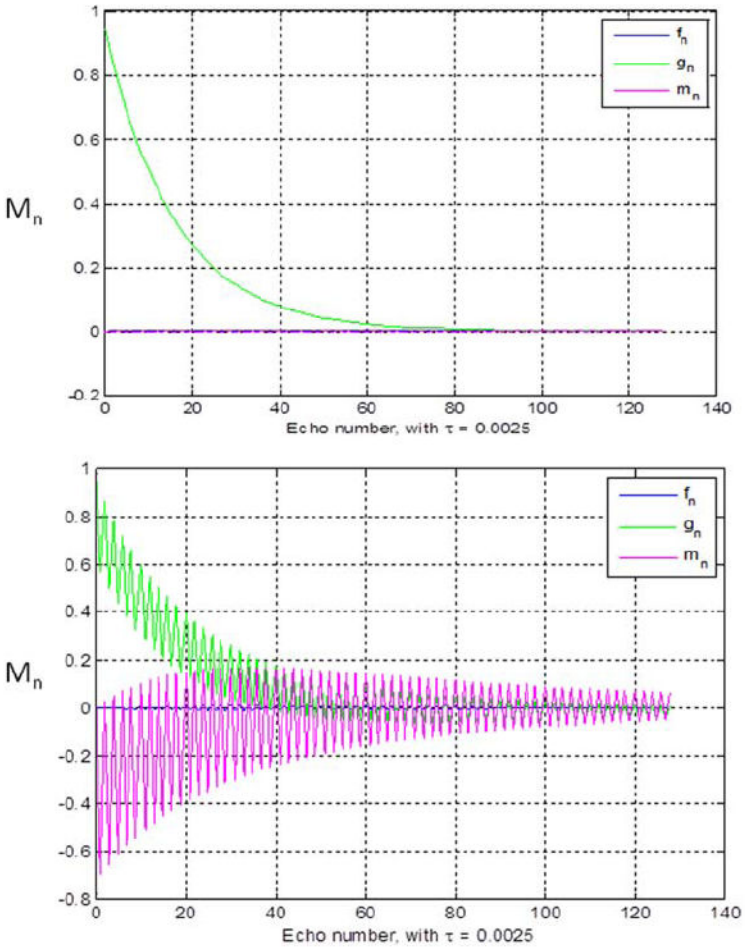

Figure 8.

Demonstration of off-resonance effects in spin echo trains when imperfect, non-180°, refocusing pulses are applied. In this case, all three components of the magnetization vector at echo centers for a 128 echo train sampled using 130° refocusing pulse flip angles are shown for a narrow range of on-resonance frequencies on-resonance (top) and for a narrow range of frequencies such that the phase of the magnetization achieves $\pi/2$ prior to the first refocusing pulse (bottom). The echo train signals were calculated assuming an R_1 and R_2 of 1 and 25 s^{-1}, respectively and an echo spacing 2τ of 5 ms.

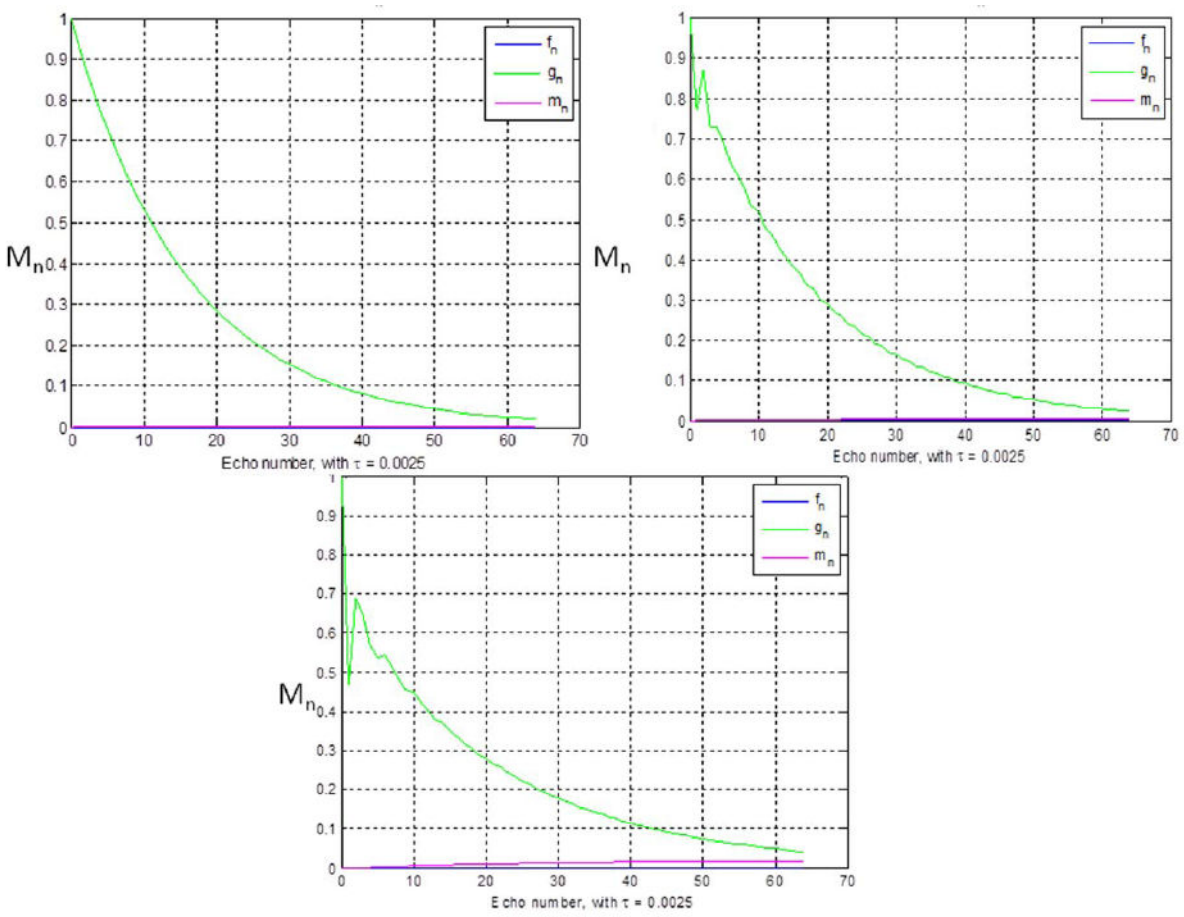

Figure 9.

In SSFSE/HASTE imaging, the frequency-encoding gradient and background gradients in lung parenchyma ensure that the off-resonance effects shown in the bottom row of Fig. 8 are smeared out. Shown are all three components of the magnetization vector at each echo center for a 64 echo train using the same tissue and sequence parameters of Fig. 8 and for refocusing flip angles of 180° (top left), 130° (top right), and 90° (bottom left) when a full range of phases from $-\pi/2$ to $\pi/2$ are achieved prior to the first refocusing pulse, as calculated using numerical integration over this phase distribution. Note the steep drop in signal for the first echo in the non-180° cases and the smooth exponential T_2 decay with a time constant of 40 ms obtained with the 180° refocusing pulses (top left).

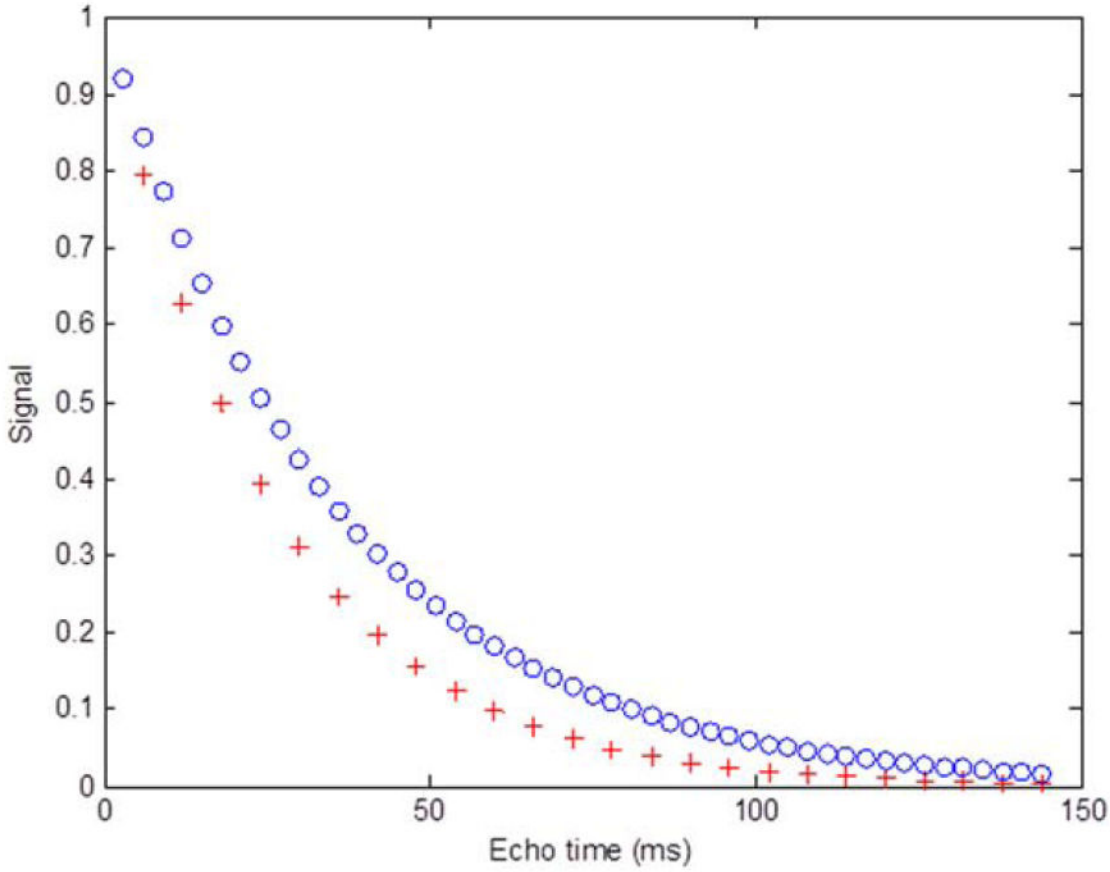

Figure 10.

Effects of echo spacing and diffusion/perfusion on pure T_2 decay curves as modulated by the diffusion term of Eq. [17]. Shown are decay curves for a 2.5 ms echo spacing (blue o's) and a 5 ms echo spacing (red +'s) as simulated using $R_2 = 25\ s^{-1}$, a D value of 10 microns^2/ms, and a G value of 8 Gauss/cm. The latter two parameters are large, with the D value corresponding to blood perfusion, or the so-called pseudodiffusion coefficient in the intravoxel incoherent motion (IVIM) model some 5 to 10 times higher than typical diffusion values (0.5 to 2 microns^2/ms). The G value employed considers additional background gradients, adding substantially to the applied readout gradients whose maxima are on the order of 3 Gauss/cm with modern scanners. One must be careful with the units when using Eq. [17] to ensure that when G is given in Gauss/cm, our preferred unit, then the diffusion coefficient D must be in cm^2/sec, not our preferred unit of microns^2/ms (1 micron^2/ms = 10^{-5} cm^2/sec).

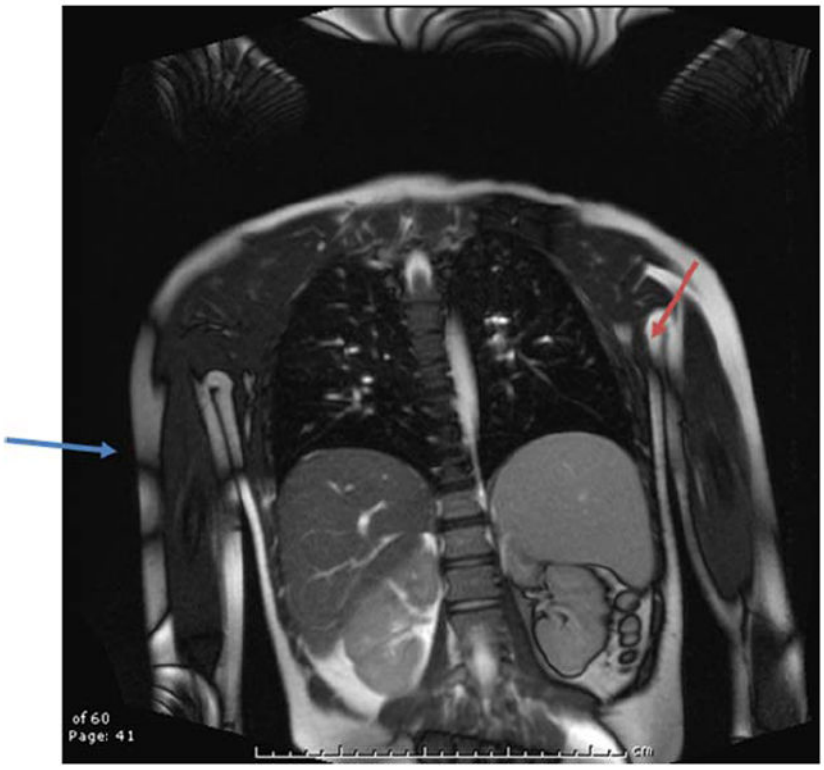

Figure 11.

A coronal bSSFP image with TR/TE 5 1.8/1.16 ms and an FA of 70°. Tissue contrast for bSSFP is complicated but generally follows a T_2/T_1 type of contrast such that blood vessels generally appear bright. Early bSSFP images suffered a great deal from the banding artifacts (arrows towards periphery of body) until repetition times could be lowered into the 5 ms range. Though the frequency dependence of the banding artifacts had been worked out decades ago, only recently have publications addressed the dependence of intravoxel frequency distributions on signal intensities, as discussed in the text and simulated for lung and other tissues (Fig. 12).

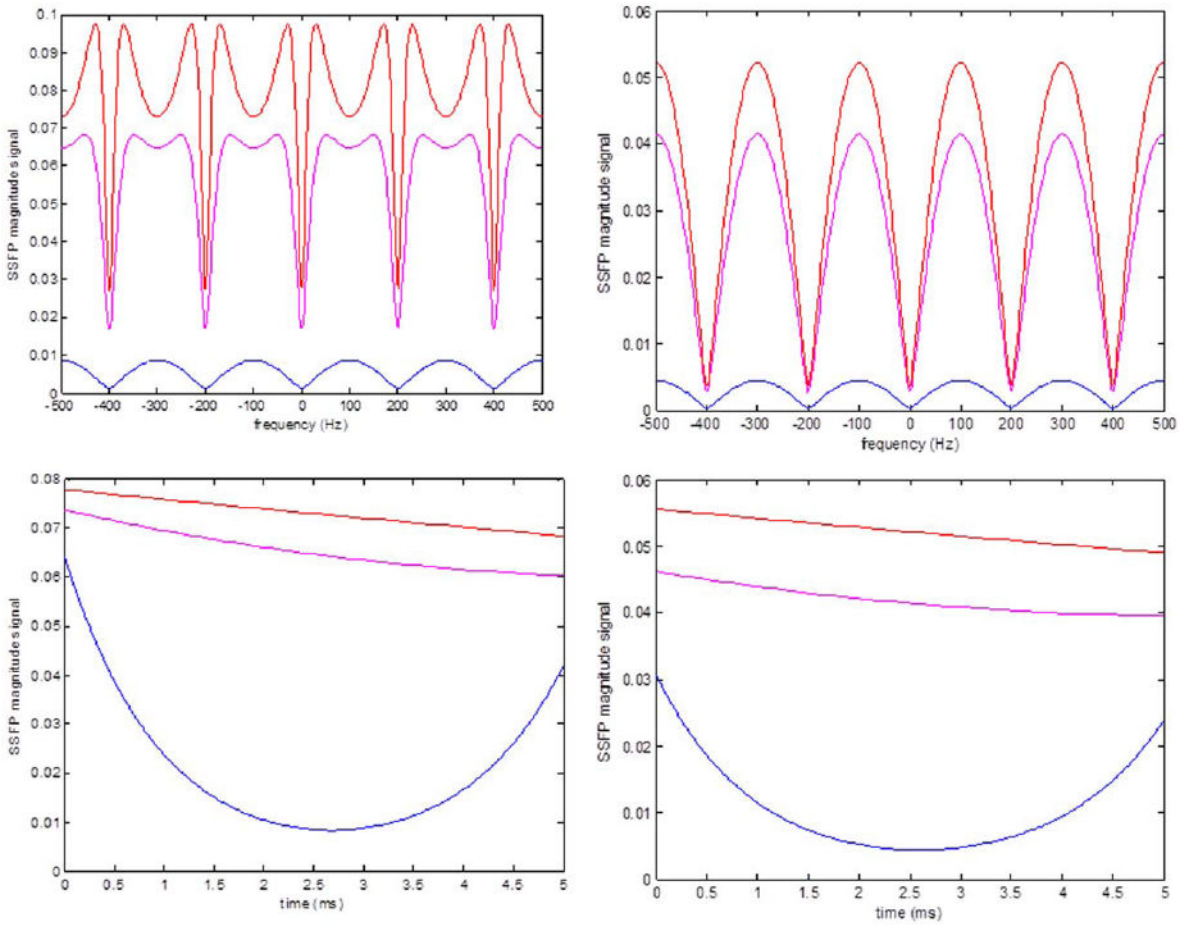

Figure 12.

SSFP frequency responses (top) for simulated muscle tissue (red), nonparenchymal lung (magenta) and lung parenchyma (blue) with a pulse spacing τ of 5 ms and the signal sampled at $\tau/2$ for low (left) and high (right) flip angles of 10° and 70°. The lower plots show the magnitude of the signal as a function of time t throughout a τ period for the passband frequency condition $w = \pi/\tau$ for the same three tissues and demonstrate that more signal from lung parenchyma would be gathered at echo times closer to the RF pulses. Table 1 has the relaxation parameters for these three tissues. We note that the lung signals have not been divided by a factor of 5 to account for air, so signal from lung tissues is overestimated by a factor of 5 in these plots for comparative visualization of the frequency (top) and time dependencies (bottom).

Table 1

Lung Parenchymal Signal Intensity in MRI

	PD	R_1 (s^{-1})	R_2 (s^{-1})	R_2' (s^{-1})	T_2* (ms)
Parenchymal components	0.1	1	25	1,000	1
Nonparenchymal components	0.1	1	25	100	8
Muscle	1.0	1	25	5	33
Fat	1.0	3.3	7	5	83
Blood	1.0	0.7	1	5	167

Proton density (PD) and relaxation parameters for the parenchymal and nonparenchymal components of lung and other major tissue components encountered in torso imaging at 1.5 T_1 (muscle, fat, and blood in large vessels) and intended as values suitable for 1.5 T simulations.